Summer 8-20-2021

Remote Sensing Identification of Black Ash (Fraxinus Nigra) in Maine Via Hyper- and Multi-Spectral Imagery

John W. Furniss
University of Maine, john.furniss@maine.edu

REMOTE SENSING IDENTIFICATION OF BLACK ASH (*FRAXINUS NIGRA*) IN MAINE VIA HYPER- AND MULTI- SPECTRAL IMAGERY

By

John W. Furniss

B.S. Elon University, 2011

A THESIS

Submitted in Partial Fulfillment of the

Requirements for the Degree of

Master of Science

(in Forest Resources)

The Graduate School

The University of Maine

August 2021

Advisory Committee:

Parinaz Rahimzadeh-Bajgiran, Assistant Professor of Remote Sensing of Natural Resources, Advisor

Aaron Weiskittel, Professor of Forest Biometrics and Modeling

John Daigle, Professor of Forest Recreation Management

Kara Costanza, Forest Pathologist, US Forest Service

REMOTE SENSING IDENTIFICATION OF BLACK ASH (*FRAXINUS NIGRA*) IN MAINE VIA HYPER- AND MULTI- SPECTRAL IMAGERY

By John W. Furniss

Thesis Advisor: Dr. Parinaz Rahimzadeh-Bajgiran

An Abstract of the Thesis Presented
in Partial Fulfillment of the Requirements for the
Degree of Master of Science
(in Forest Resources)
August 2021

North American ash species (*Fraxinus* spp.) are under dire threat from the invasive pest, emerald ash borer (*Agrilus planipennis*, EAB). Black ash (*F. nigra*) has shown no resistance to EAB while its cultural and ecological importance render it irreplaceable. Traditional field forestry techniques are not suitable for the large-scale identification of individual black ash trees to facilitate conservation, thus necessitating the need for other identification and classification techniques. The objective of this research is to develop remote sensing techniques that can be used to identify ash trees, in particular black ash, at the individual tree level using both hyperspectral and multispectral data. Both general ash species identification and black ash tree identification in a low-density mixed forest using hyperspectral data have not been reported in the literature. Specifically, this study aims to use optical remote sensing data to: 1) create a pixel-based classification model for ash tree identification, 2) develop an object-based classification model for ash tree identification, and 3) use the most accurate ash tree classification model as a basis for a black ash tree classification model.

Analysis of spectral differences between classes suggests that both ash in general and black ash specifically can be successfully separated from co-occurring species. Where

classification models were significantly different, object-based methods performed better than pixel-based methods and Support Vector Machine (SVM) models generally outperformed Random Forest (RF). The highest accuracies were achieved using object-based methods and hyperspectral data, although multispectral data were able to successfully differentiate ash as well. Using object-based, SVM methods, black ash was successfully differentiated from co-occurring hardwood species using both hyperspectral and multispectral data, with hyperspectral data achieving 70% Producer's and 70% User's Accuracy for black ash and multispectral data achieving 57% and 50%, respectively.

Despite relatively low sample sizes, this research presents a viable path forward with respects to black ash mapping. As this study shows, black ash can be successfully differentiated from closely related species using remotely sensed optical data. While capturing hyperspectral data is likely cost prohibitive for large-scale mapping efforts, multispectral sensors are more viable and can achieve similar results. At a minimum, the techniques presented in this research can be used to assist and guide field conservation work to locate areas of high likelihood of black ash presence so that they can be identified and informed decisions made about their preservation.

TABLE OF CONTENTS

LIST OF TABLES

LIST OF FIGURES

CHAPTER 1 INTRODUCTION

The increasingly interconnected nature of the global economy has led to a period of unprecedented movement of people and goods throughout the world. As has been the case throughout history, this intentional movement is accompanied by the unintentional movement of certain organisms linked to the goods. Of particular interest are invasive species that are able to separate from their mode of transport and colonize a new location. These species can create immense problems, as they typically have few (if any) predators in the new environment and can usually outcompete local species. In other situations, the invasive species may have co-evolved with a certain genus within its native range where it is harmless, but when presented with members of that genus in a new range, can cause mortality. Such is the case with emerald ash borer (*Agrilus planipennis*, EAB) and native ash tree species (*Fraxinus* spp.) in North America.

1.1. Ash tree ecology and importance in Maine and North America

In North America, there are sixteen native ash tree and shrub species, of which three are present in Maine, United States. These species – white ash (*F. americana),* green ash (*F. pennsylvanica*) and black ash (*F. nigra*) - make up vital components of much of the hardwood forests in Maine, United States. Overall, three ash species account for roughly 4% of Maine's hardwood forests, and the estimated value of ash trees in Maine is approximately $320 million (Maine Forest Service 2018). Ash serves many uses, with white ash being used in goods such as baseball bats and boat oars, and green ash being a (formerly) commonly planted urban tree in many environments (Kennedy 1990). Black ash, while ecologically and culturally important, has few "lumber" uses besides flooring and is not hardy enough to plant in urban settings (Wright and Rauscher 1990).

Ash trees serve many important ecosystem functions. Green and white ash typically produce large amounts of seeds for a variety of birds, small mammals, and insects to feed on, while the browse and thermal cover are valuable for larger mammals such as deer and moose (Cappaert et al. 2005). White ash can be found over much of the eastern United States as far west as eastern Texas and Minnesota, as far south as the Florida panhandle, and north into Maine and Nova Scotia in Canada. While white ash almost never is the dominant species in a forest, it is a major component of the White Pine-Northern Red Oak-Red Maple forest type and a common component of 25 other different forest cover types. The range of green ash is even greater, extending to southeastern Alberta in Canada, southeastern Texas, northwestern Florida, and northeast to Cape Breton, Nova Scotia in Canada. Similar to white ash, green ash is an integral component of the Sugarberry-American Elm-Green Ash forest cover type and is an associated species of 22 other forest cover types (Burns and Honkala 1990). In addition to their traditional ecosystem roles, green and white ash have become some of the most commonly planted trees in urban and suburban settings, with researchers estimating that ash comprised over 20% of planted trees in many areas of the country (Kovacs et al. 2010). The range of black ash is restricted to the area surrounding the Great Lakes and east into New England and the Canadian Maritime provinces. It is an integral part of the black ash-American elm-red maple forest cover type, a common associate of one other forest type, and a minor associate of four (Burns and Honkala 1990).

From an economic perspective, ash is a critical resource for much of the eastern United States. As of 2003, ash made up roughly 7.5% of hardwood sawn timber, the undiscounted stumpage price of forest ash was estimated to be $25 billion, and the compensatory value was above $280 million (Federal Register 2003). Potentially more impactful, however, has been

various ash species' use as ornamental trees in urban settings. Many ash trees were planted in the wake of Dutch elm disease (*Ophiostoma* spp.), with both green and white ash being planted extensively and some cities such as New York, Oakland, Boston, and Chicago having over 14% of leaf area in ash trees before the introduction of EAB (Federal Register 2003; Poland and McCullough 2006). Researchers in the Midwestern United States estimated that the loss of ash could cost communities as much as $395,000-$769,000 per 1,000 residents, for a total loss of between $13.4 and $26 billion (Sydnor et al. 2011).

1.1.1. Black ash ecology and importance in Maine

Black ash is a central part of several Native American teachings and is a vital component of many mixed forests in Maine. It has been used by members of Native American tribes in New York, New England, and southeastern Canada to make baskets for generations – whether the larger, sturdy baskets used for gathering or the smaller, intricate baskets designed to provide revenue – and forms a part of the Wabanaki creation story (Costanza et al. 2017). Furthermore, black ash inhabits a unique ecological niche – it can colonize extremely wet sites and yet is very drought tolerant (Burns and Honkala 1990). It is typically found well distributed in areas with soil wet enough to allow black ash to outcompete other vegetation but grows best in areas that are wet because of proximity to water (such as flood plains or river terraces) rather than due to poor soil drainage (Costanza et al. 2017).

In Maine, black ash is typically found in wetlands and along rivers as part of the black-ash-balsam fir-American elm forest type, although with the prevalence of Dutch elm disease, elm (*Ulmus americana*) is often replaced by red spruce (*Picea rubens*) or red maple (*Acer rubrum*) on drier sites (Burns and Honkala 1990) and black ash on wetter ones (Costanza 2015). It is a dioecious tree, meaning that the tree reproduces sexually and cross-pollination is required for

successful germination. In addition, black ash rarely produces good seed years, with only 11 "good" seed years occurring over a 35-year study (Erdmann et al. 1987). Further, while black ash can sprout prolifically from stumps, the density of black ash in a stand seems to decline as the trees mature and become more shade intolerant (Erdmann et al. 1987). Should the trees remain seedlings, however, they can persist for years with little to no growth (Klooster et al. 2018).

The unique element of black ash ecology, at least amongst the ash species, is its effect on the hydrology of a site. Black ash is well suited to growing in extremely wet sites, with a number of key adaptations – including hypertrophied lenticels allowing for extremely high rates of evapotranspiration – that allow it to thrive where other species simply cannot. In certain areas, such as the western Lake States, this can lead to vast stretches of forested wetlands dominated by black ash (Kolka et al. 2018). In very wet areas such as these, the very presence of black ash actually controls the water table and allows other tree species to colonize the site (Slesak et al. 2014). In small areas, loss of enough black ash has been linked to loss of forest cover itself, as the loss of transpiration causes the water table to rise high enough to eliminate trees from the site (Erdmann et al. 1987; Youngquist et al. 2017). Whether the loss of forest cover will translate to a landscape scale remains to be seen, however, as more recent studies have shown that the effect may be more muted than originally suggested and possibly nonexistent if less than 20% of the black ash basal area is removed (Slesak et al. 2014).

1.1.2. Emerald ash borer (EAB) outbreak in North America and its impact in Maine

EAB was first identified in North America in Ontario, Canada and Michigan, United States. in 2002 but is suspected to have been present for longer (Siegert et al. 2014). EAB damages trees by tunneling areas under the bark, producing girdling wounds that interfere with water and nutrient movement, which indirectly leads to canopy defoliation. Endemic to China,

EAB does not cause mortality in the ash trees of its native range as the trees have developed high levels of tannin in defense (Rebek et al. 2008), but when introduced to North American ash trees it has caused widespread mortality in native ash species – up to 99% over 5-10 years (Herms and McCullough 2014). Attacked trees will usually be dead within three years, although mortality within the first two years is possible when the EAB population level peaks (Haack et al. 2002). Colonization typically begins in the upper part of the canopy, allowing damage to escape early detection. EAB has been shown to colonize otherwise fully healthy ash trees anywhere from 4 cm to over 1 m in diameter, even killing irrigated and fertilized ash trees in southeastern Michigan (Herms and McCullough 2014). There are four key life stages for EAB (Figure 1.1).

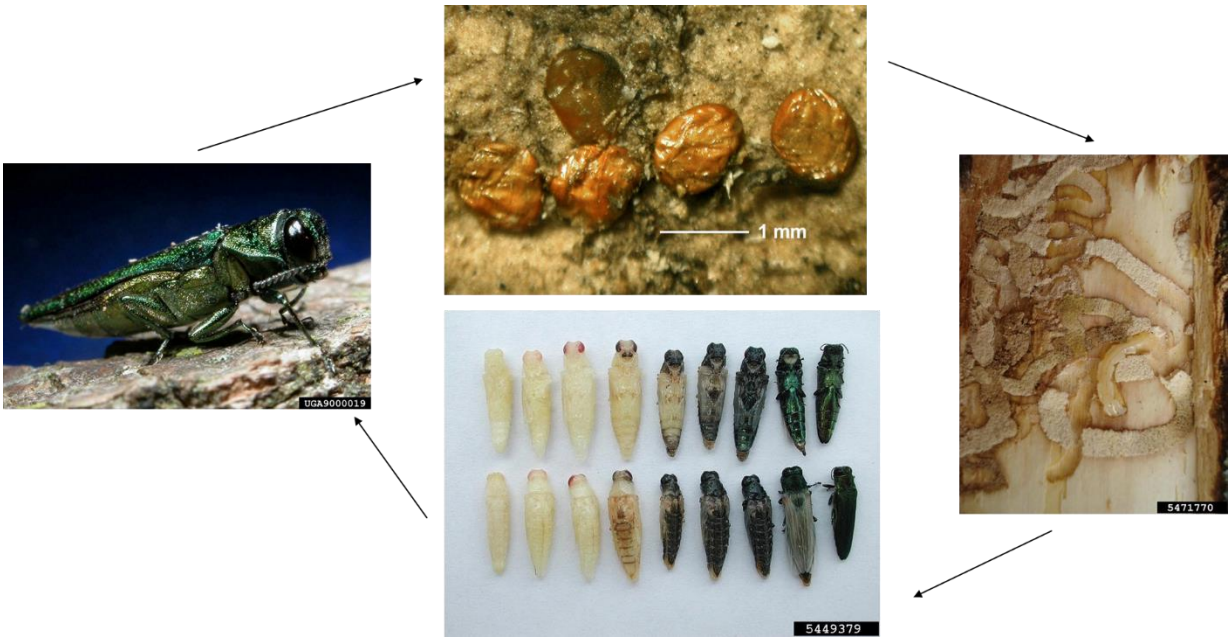

Figure 1.1 EAB life stages. Clockwise from top: egg, larva + galleries, pupa, adult
Eggs: David Cappaert, Bugwood.org
Larva + galleries: Kenneth R. Law, USDA APHIS PPQ, Bugwood.org
Pupa: Debbie Miller, USDA Forest Service, Bugwood.org
Adult: David Cappaert, Bugwood.org

Since its introduction in the early 1990's, EAB has spread rapidly throughout the continental United States and Canada (Herms and McCullough 2014). Like many pests it relies

on mixed-dispersal methods, with the beetle able to cover short distances by flight and long distance dispersal occurring via human transport of infested materials (Mercader et al. 2011).While Prasad et al. (2010) estimated that EAB has been spreading along a front at roughly 20 km/year, much of that is dependent on human facilitated transport of infested materials. Flight mill experiments have suggested that EAB adults are capable of traveling nearly 10 km during their lifespan (Taylor et al. 2007), however such studies are difficult to relate to real-world abilities. Mercader et al. (2009) found roughly 90% of larvae were on trees within 100 m of the adult emergence site (with the overall pattern fitting a negative exponential function), suggesting a much more limited range of unassisted dispersal.

As those areas initially infested by EAB have begun to see some regeneration, valuable information is being gleaned from the long-term effects of EAB on a landscape. With over 99% initial ash tree mortality, when EAB infects an area large gaps will begin to form in the canopy (Klooster et al. 2018) thereby greatly increasing the amount of light available on the ground, potentially leading to successional changes. This can be especially true in undisturbed black ash forests, where the continuous recruitment of ash allows for small gaps, but not large ones, to form. Furthermore, due to its ability to colonize extremely wet sites and the presence of hypertrophied lenticels allowing for extremely high rates of evapotranspiration (Tardif et al. 1994), the removal of black ash from a site can cause drastic hydrologic effects. Slesak et al. (2014) found that once these forested wetlands had black ash removed from the site, they became marshes with little to no tree cover.

Unfortunately, even the decimation of a site's ash population is not a remedy to eliminating EAB. As EAB kills the overstory trees, the ash seed bank also becomes depleted as trees are killed before they can reproduce. This leads to an "orphan cohort" of ash that are too

small to produce seeds or be infested by EAB. As these trees mature a certain number will become large enough to be infested by EAB, thereby allowing EAB to persist in the environment (Klooster et al. 2014). Therefore, once a stand has been infested it must be monitored for years to make sure that no further outbreaks occur.

There are multiple EAB monitoring efforts employed including trap trees, green and purple prism traps, and funnel traps (Francese et al. 2019; Maine Forest Service 2020; Poland et al. 2019). In Maine, active monitoring of most ash sites is difficult or impossible, as the dispersed nature of ash growth in the state makes finding significant populations of ash difficult and time consuming to begin with (Everett 2019). Furthermore, the sites on which black ash are most commonly found – that is, swamps and wet lowlands - can present additional logistical difficulties. Due to the high water table many sites are inaccessible for parts of the year and, even when accessible, traditional surveys would require trained crews covering large areas of difficult terrain looking for small trees (Burns and Honkala 1990) that can reach the canopy while being less than 10 cm in diameter (J. Furniss, *Personal Observation*). As such, many attempts to map ash at a large scale using traditional forestry techniques run into the issues of time and labor that present profound difficulties. Therefore, alternative methods such as remote sensing techniques must be considered.

1.2. Remote Sensing of Forests

For a long time, both space- and air-borne remote sensing sensors have been used for various forestry applications from forest type and composition classification (Thapa et al. 2020; Wolter and Townsend 2011), forest disturbance (Cohen et al. 2017; Hall et al. 2016; Rahimzadeh-Bajgiran et al. 2018), and productivity estimation (Rahimzadeh-Bajgiran et al. 2020). Landsat satellite program has over 45 years of image availability and Landsat data have

been used extensively for vegetation studies. As early as 1980, researchers and forest industry companies were partnering to develop forest type maps for northern Maine using Landsat (Bryant et al. 1980). While the coarse resolution of Landsat data (30 m) is suitable for landscape level forest type mapping, the increasing availability of very high spatial resolution data has shifted focus towards identifying individual trees at a species level (Fassnacht et al. 2016). Researchers have developed an increasingly large number of techniques and data sources to achieve individual tree species identification – from spectral bands and spectral vegetation indices (SVIs) to LiDAR (Light Detection and Ranging) based texture metrics (Fassnacht et al. 2016; Marrs and Ni-Meister 2019).

There are numerous satellite and aerial active and passive remote sensing sensors available. The passive sensors are classified into multispectral and hyperspectral sensors. In this study we intend to examine data from one multispectral high resolution space-borne (Worldview-2, WV-2) and one hyperspectral high resolution air-borne (Goddard's LiDAR, Hyperspectral, and Thermal imager, G-LiHT) sensor –to assess their respective potential for ash tree identification. Each data set has its own benefits and limitations; for example, multispectral data are typically less expensive and easier to acquire (at least for the data sets examined in this study) compared to hyperspectral data. The limitation, therefore, is in the amount of spectral data acquired; multispectral imagery is only gathered in a limited number of spectral bands, as opposed to the hundreds captured in hyperspectral imagery. Furthermore, the finer spectral resolution with which hyperspectral data are gathered allows for the significantly increased ability to calculate different spectral indices, which may be useful in differentiating between plant species. However, pre-processing and analyzing hyperspectral data are more challenging. Thus, tradeoffs in spatial and spectral resolution must be made between the data sets.

WV-2 satellite sensor provides multispectral images in eight spectral bands (red (659 nm), green (546 nm), blue (478 nm), coastal blue (427 nm), yellow (608 nm), red-edge (724 nm), near-infrared 1 (831 nm), and near-infrared 2 (908 nm)) at roughly 1.84 m spatial resolution and a panchromatic band at roughly 0.46 m resolution (DigitalGlobe 2009). Hu et al. (2018) found that red-edge bands from Worldview-3 (WV-3) and structural indices derived from the panchromatic band significantly improved ash tree identification. While WV-3 has slightly higher spatial resolution than WV-2 (0.31 m in the panchromatic band compared to 0.46 m, respectively), the WV-2 pixel sizes are significantly smaller than the average tree crown widths in Maine (Russell and Weiskittel 2011) and so should be sufficient to generate helpful structural data (Li et al. 2015). It should be noted that WV-3 imagery was not used in this study due to there being no available imagery of the study area during the late spring, summer, or early fall (June – September).

G-LiHT data come from NASA Goddard's LiDAR, Hyperspectral, and Thermal airborne system, capturing hyperspectral data at a 1.5 nm spectral and 0.6 m spatial resolution (Cook et al. 2013) in up to 185 spectral bands with 400-1000 nm spectral range. This sensor package is highly flexible, as it can be mounted on several different types of small planes, and, while not directly addressed in this study, the addition of concurrently gathered LiDAR and thermal data allow for greatly increased data accuracy and analysis options. More relevant to this study, the hyperspectral data such as that gathered by the G-LiHT system have been shown to aid in the identification of ash trees (Liu 2017) and in predicting ash tree health (Pontius et al. 2008).

1.2.1. Tree identification using optical hyperspectral and multispectral remote sensing data

As the available data sources and applications of remote sensing have multiplied, so have the approaches taken. In certain situations, examining the relationships and ratios between

spectral bands reflectances – in the form of calculated SVIs– can either be used to provide greater amounts of information and identification power (Bhattarai et al. 2021; Pontius et al. 2017) or simply to reduce the amount of data being processed (Fassnacht et al. 2016). SVIs can range from simple ratios between two spectral bands to complex formulas involving multiple spectral wavelengths and constants with efforts made to account for multiple compounding variables, such as the effect of soil reflectance (Ishimura et al., 2011; Xue and Su 2017). In general, SVIs derived from multispectral data are less sensitive to small changes in biophysical parameters and vegetation structure but also less susceptible to external factors such as illumination and atmospheric conditions than comparable hyperspectral SVIs (Jones and Vaughan 2010).

There are numerous techniques for identifying objects, in particular trees, in a remotely sensed image based on the optical properties of the image (Fassnacht et al. 2016). Specifically, the amount of radiation reflected at different wavelengths (and the ratios between those amounts) are indicative of plant chemical properties, leaf morphology, and canopy structure. For example, by examining how much the reflectance changes from pixel to pixel it is possible to determine whether the trees are broadleaved (deciduous) or needle-leaved (coniferous) (Ferreira et al. 2019). Further, by utilizing the spectral data researchers are able to create signatures for individual tree species. Much like a human fingerprint, each tree species will have a specific reflectance based on leaf pigment content and canopy structure that, in theory, makes it possible to identify (Dalponte et al. 2014). There is, however, significant overlap in spectral signatures even between trees of unrelated species, such as that between sycamore maple (*Acer pseudoplatanus*) and European common ash (*Fraxinus excelsior*) (Lisein et al. 2015), that make identification using purely spectral means difficult. However, as the spatial resolution of

remotely sensed data is increased, pixel sizes have decreased to the point where one canopy likely covers numerous pixels. As such, examining each individual pixel may not produce the best classification results because the variability within the tree crown will be significantly less than the variation between the crown and surrounding pixels (Immitzer et al. 2012). Such small pixel sizes allow for the calculation of inter- and intra-crown texture metrics (such as homogeneity or variance), which researchers have included along with spectral data to increase accuracy of models (Franklin et al. 2000). To facilitate accurate comparisons of tree species, researchers have developed techniques to group pixels into crowns for easier identification (Ma et al. 2017).

Researchers have developed many techniques for the delineation of individual tree crowns (ITC) which generally fall into two categories, object-based or pixel-based (Myint et al. 2011). Pixel-based delineation systems commonly work by identifying the most likely identity of each pixel, while object-based delineation systems use different methods to group pixels into "objects," which are then classified. Object-based systems have been shown to improve recognition of landscape level features (Blaschke and Hay 2001) as well as trees (Myint et al. 2011). While there are numerous methods for automatically delineating ITCs including valley-following (Gougeon and Leckie 2006) and region growing (Bunting and Lucas 2006), multiband watershed segmentation techniques have been shown to have more success in mixed species forests than either other method (Yang et al. 2014a). Traditional watershed segmentation techniques use a single spectral band or grayscale image to effectively create a topographic relief of the area, which is then divided into a series of catchment zones (Beucher 1982). As such approaches are based on a single spectral band, however, they fail to take advantage of the majority of data derived from sensors. Recent studies have found that, by using the spectral angle

[a common metric to describe the difference between the spectra for two pixels, (Sohn and Rebello 2002)] for watershed segmentation rather than an individual spectral band, accuracy can be greatly improved (Yang et al. 2014a).

Once the classification objects are obtained (whether individual pixels or segmented objects), researchers use a variety of classification algorithms to assign a class to each object. Similar to ITC delineation, classification algorithms fall into two broad categories – parametric and non-parametric. Parametric algorithms, like maximum likelihood classification and linear discriminant analysis, assume a normal distribution of data and rely on parameters derived from training data, however they can result in noisy results in a complicated environment (Lu and Weng 2007). Non-parametric algorithms, such as Support Vector Machine (SVM) and Random Forests (RF), do not make any assumptions about the data, and may produce better results in a complex landscape (Foody 2002). Many studies have used either the SVM method (Marrs and Ni-Meister 2019; Nitze et al. 2012; Thanh Noi and Kappas 2018) or the RF classifier algorithm (Bhattarai et al. 2021; Immitzer et al. 2012; Lisein et al. 2015; Murfitt et al. 2016) or - we intend to compare the two to determine optimum classification ability.

1.2.2. Remote sensing identification of ash using hyperspectral and multispectral data

Due to the dispersed growing pattern of ash in Maine and the predominance of other tree species, the majority of current research focuses on detecting ash at the genus level and has mostly used high resolution single-date multispectral satellite (Murfitt et al. 2016; Sapkota and Liang 2020) or multi-temporal aerial imagery to identify ash (Lisein et al. 2015). Murfitt et al. (2016) used WV-2 multispectral satellite imagery (8 bands, ~0.5 m resolution) to achieve an overall accuracy of roughly 63%, while Sapkota and Liang (2020) used WV-3 imagery (5 bands, ~0.3 m resolution) and achieved an overall accuracy of 82%. Further, Lisein et al. (2015)

reported an out-of-bag error rate of 17% using single-date drone captured multispectral data (4 bands, ~0.2 m resolution), but decreased their error to 13% when multiple dates were used. Single-date high resolution hyperspectral imagery has been found to be promising in identifying ash trees in an urban environment, with Pontius et al. (2017) achieving 81% accuracy.

While the majority of studies have continued to focus on mapping ash at the genus level, there has been recent interest in mapping black ash at the landscape level, specifically in the Lake States (Michigan, Minnesota, and Ohio, among others). These studies have had success in mapping black ash dominated stands using medium resolution multispectral satellite imagery with Engelstad et al. (2019) achieving 14.5% error (85.5% accuracy) using single-date Landsat-derived SVIs combined with LiDAR-derived topography (30 m resolution) and Host et al. (2020) achieving 72% accuracy using Landsat and Sentinel-2 (10 m resolution) time-series to map black ash. In parallel, the US Forest Service has developed Individual Tree Species Parameter Maps with the aim of predicting the density of a given tree species in order to determine insect or disease risk (USDA Forest Service 2018). Similar to the previous studies, these maps are based on Landsat 30 m resolution data and incorporate climate, terrain, and soil data in addition to ground truth data. The ground truth data, however, is obtained through the Forest Inventory and Analysis program, which utilizes a method of sampling known to underestimate black ash abundance (Everett 2019). As such, while these methods can prove to be a helpful starting point (the Individual Tree Species Parameter Maps, in particular, as they cover the entire United States) in mapping black ash, the underlying data are unsuitable for mapping black ash at the individual tree level.

While other studies – namely Pontius et al. (2017) – used spectral unmixing methods such as mixture tuned matched filtration, such methods present a challenge in Maine. These

techniques rely on identifying pure pixels of the target sample, otherwise known as pure endmembers, and then classifying pixels based on how closely they match the endmembers. With the scattered nature of ash tree distribution and a complex understory, it is hard to find a pure ash pixel, thereby greatly limiting spectral unmixing's applicability in Maine. Demonstrating the technique's reliance on pure pixels, Pontius et al. (2017) found that only the most vigorous crowns (providing the purest ash crown pixels) were accurately categorized (62%) with all other classes produced under 25% accuracy. A more recent study by Sapkota and Liang (2020) utilized object-based methods to achieve 82% accuracy in mixed hardwood stands more similar to Maine's mixed forests than the urban environment studied in Pontius et al. (2017), suggesting that spectral unmixing is not required.

In this study we aim to use high resolution multispectral and hyperspectral data to identify ash trees in a non-urban setting with a focus on black ash, for the first time differentiating black from other ash species at the individual tree level.

1.3. Research problem

Somewhat contrary to early predictions, there has been emerging evidence for EAB resistance in both white (Steiner et al. 2019) and green (Klooster et al. 2018) ash. Unfortunately, there have been no such findings for black ash (Klooster et al. 2014), suggesting that it remains vulnerable. However, the majority of studies concerning EAB-caused ash mortality have occurred in the Lake States where black ash grows very differently than in Maine. In the Lake States, black ash tends to form pure stands on very wet sites with few (if any) other canopy species, while white and green ash tend to be more dispersed throughout the forest (Klooster et al. 2014). While Maine does not have the same level of black ash dominance, there is a region of Maine known as the "Ash Belt," roughly running from Waterville through Bangor and Lincoln

to Houlton, where there are larger concentrations of ash (Tyler Everett, *Pers. Comm.*). The region around Lincoln, Millinocket, and Houlton has high levels of black ash in particular, along with the co-occurring species of red maple and northern-white cedar (*Thuja occidentalis*). Throughout the rest of Maine, however, black ash tends to grow in a more dispersed pattern that has been shown to convey a modest amount of protection from EAB (Knight et al. 2013), however the lack of any evidence for black ash survival remains extremely concerning.

Due to their spatially dispersed growing pattern, damage to black ash trees can be difficult to identify via remote sensing techniques. Furthermore, the particular life cycle of EAB makes mapping current infestations problematic. By the time noticeable defoliation occurs the larvae are typically in the second year of their life cycle and about to emerge as adults (Herms and McCullough 2014). At this point it is unlikely that the tree can be saved, as the population of EAB will have grown significantly - females can lay 50-90 eggs during their lifetime (Poland and McCullough 2006) – and the tree can serve as a new source of infestation.

Most current methods have focused on using remote sensing techniques to identify ash at the genus level with a focus on tree decline and mortality, either with multispectral data in hardwood dominant forests (Engelstad et al. 2019; Murfitt et al. 2016; Waser et al. 2014) or with hyperspectral data in urban environments (Pontius et al. 2017; Pontius et al. 2008). Finally, even when studies aim to directly map black ash densities, they are at far higher densities (over 50% stand basal area in black ash) and spatial scales (30 m resolution) that are not applicable to the situation in Maine (Engelstad et al. 2019; Host et al. 2020), or rely on data unsuitable for individual tree identification (USDA Forest Service 2018). As EAB has not currently been detected in central Maine, we hope to identify pre-infestation ash populations for monitoring and conservation purposes. Finally, while researchers are examining different tree species for their

ability to replicate the effect of black ash on wetlands, there is no true possible replacement for black ash's cultural significance (Costanza et al. 2017; D'Amato et al. 2018).

1.4. Research objectives

Goal: To identify ash trees in Maine from remote sensing data.

- Objective 1: Create and evaluate pixel-based classification models for tree species identification using multispectral and hyperspectral remote sensing variables in Maine.
    - Hypothesis 1: Certain spectral band or wavelength combinations (SVIs) will result in higher classification accuracy than others
    - Hypothesis 2: Hyperspectral data result in higher classification accuracy compared to multispectral data
- Objective 2: Create and evaluate object-based classification models for tree species identification using multispectral and hyperspectral remote sensing variables in Maine.
    - Hypothesis 1: Object-based classification methods yield higher classification accuracy compared to pixel-based classification methods
    - Hypothesis 2: Hyperspectral data result in higher classification accuracy compared to multispectral data
- Objective 3: Identify the set of other variables that results in the optimum differentiation of black ash from green and white ash species using single-date imagery
    - Hypothesis: Using a set of derived variables (such as SVIs) will result in higher classification accuracy than using multispectral or hyperspectral single bands alone

1.5. Thesis structure and overview of each chapter

This thesis is broken up into four chapters. This chapter (Chapter 1) provides background on the importance of ash and its vulnerability to EAB, as well as introductory information on the history of remote sensing and its application to the identification of single trees within a forest. In addition, Chapter 1 outlines the research need, thesis objectives, and originality of research. The information presented in this chapter forms the foundational background for the research methods presented in Chapters 2 and 3.

Chapter 2 focuses on using hyperspectral imagery to classify ash and associated species, utilizing both pixel- and object-based classification methods. Chapter 3, likewise, focuses on using multispectral data with both pixel- and object-based classification methods. In both cases, accuracy assessments of all models are presented and the most accurate classification methods are then used to map black ash trees. Finally, Chapter 4 integrates the previous chapters, providing recommendations on the most accurate classification achieved, possible avenues for future research, and discussion of the real-world applications of this research.

CHAPTER 2 MAPPING ASH SPECIES ACROSS A MIXED FOREST USING HYPERSPECTRAL IMAGERY

2.1. Introduction

One essential component in active monitoring of EAB infestations is mapping ash tree distribution. Due to the dispersed growing pattern of ash and the predominance of other tree species, high spatial resolution remote sensing data are needed to identify ash trees at the genus level (Lisein et al. 2015; Murfitt et al. 2016; Sapkota and Liang 2020). Hyperspectral data have been used to identify tree species in numerous settings (Amini et al. 2018; Dalponte et al. 2014; Garzon-Lopez and Lasso 2020), and have been used to identify ash trees in urban settings in the United States (Pontius et al. 2017) and in forested areas in Europe (Maschler et al. 2018).

In this study we intend to examine data from G-LiHT to assess their potential for ash tree identification. G-LiHT captures hyperspectral data at a 1.5 nm spectral and 0.6 m spatial resolution (Cook et al. 2013) in up to 185 spectral bands with 400-1000 nm spectral range. The fine spectral resolution with which hyperspectral data are gathered allows for the significantly increased ability to calculate different SVIs, which may be useful in differentiating between plant species. More relevant to this study, the hyperspectral data such as that gathered by the G-LiHT system have been shown to aid in the identification of ash trees (Liu 2017) and in predicting ash tree health (Pontius et al. 2008).

While this is not the first attempt to use hyperspectral imagery to identify ash at the individual tree level (Maschler et al. 2018; Pontius et al. 2017; Zhang et al. 2012), this is the first attempt to differentiate ash species (black, green, and white) from one another in a mixed-forest environment. Previous studies such as Pontius et al. (2017) focus on ash in urban settings, while others such as Liu (2017) and Zhang et al. (2012) are focused on predicting ash health. One study, Maschler et al. (2018), used similar hyperspectral data to identify ash and co-occurring

species in Austria. Critically, however, they employed only object-based techniques and utilized a LiDAR-derived canopy height model, whereas this study will rely on optically-sensed data. Finally, to our knowledge the attempt to use G-LiHT hyperspectral data to differentiate ash species at the individual tree level presented in this study is novel and represents an original approach. The main goal of this Chapter is to map forest composition at tree level in a forested area in Maine having ash trees at different densities and to separate black ash from other ash species using G-LiHT hyperspectral imagery. The specific objectives are: 1) create and evaluate both pixel-based and object-based classification models for tree species identification with the focus on ash tree identification and 2) evaluate different non-parametric algorithms for tree identification.

2.2. Materials and methods

2.2.1. Field work

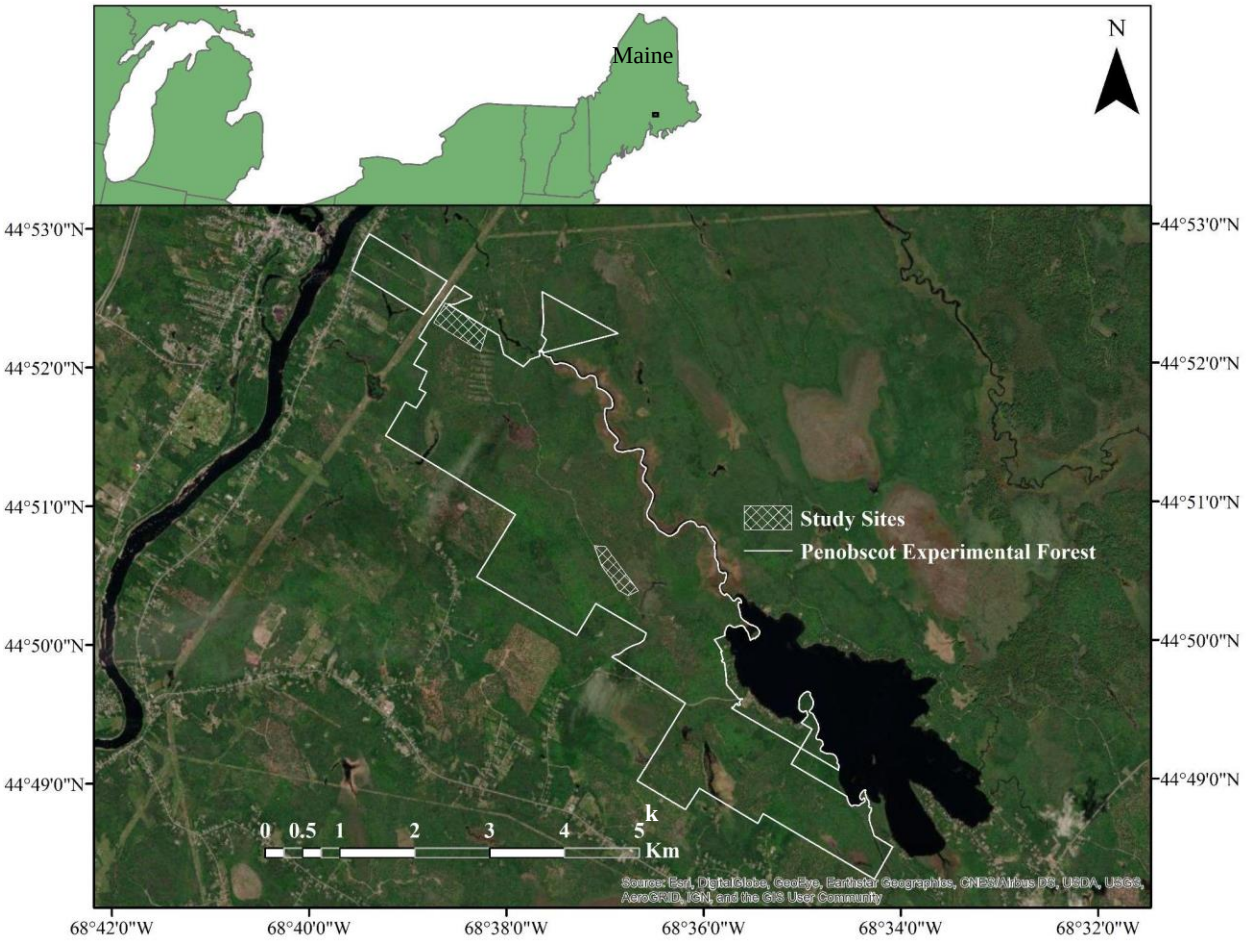

Figure 2.1 Map of Penobscot Experimental Forest, Bradley, Maine, United States, with study sites

The Penobscot Experimental Forest (PEF) (44°85'20"N, 68°62'00"W; (Figure 2.1), is part of the Northern Research Station of the US Forest Service and located in Bradley, Maine, United States. It has been identified as an area that has measurable populations of ash, as well as readily (and freely) available field inventory and remote sensing data (such as G-LiHT and National Agriculture Inventory Program [NAIP] imagery). We identified Management Unit 2 (hereafter referred to as Site 1), along with another area in the southern part of the PEF (Site 2),

as being sites potentially higher in ash and, in particular, black ash density.[1] These sites also had high rates of typically co-occurring species with black ash, such as balsam fir (*Abies balsamea*), paper (*Betula papyrifera*) and yellow birch (*B. alleghaniensis*), northern white cedar, and red maple, making the presence of ash more likely.

In Site 1 (22.5 ha), a preliminary survey was conducted by setting out four transects spaced 75 m apart running lengthwise (approximately 700 m) through the site. A visual scan of each side of the transect was conducted to identify all canopy dominant or co-dominant ash trees (Figure 2.2.b) – pairs of researchers would walk one on each side of the transect approximately 10-15 m apart and only be responsible for their side of the transect. Scanning distance was limited by visibility (Figure 2.2.a) and no defined distance limit was placed. Species spot checks within pairs of researchers served as a check against misidentification.

Figure 2.2 Selected photos from field. Clockwise from top left a) example section of study site b) black ash in canopy, c) black ash, diameter at breast height 12.7 cm (5 in), and d) GPS located black ash trees

[1] A third potential site was identified in the northern portion of the PEF but was eventually dropped due to difficulty of access and lack of observable black ash.

Based on preliminary surveys of Site 1, transects were clustered into the areas of higher ash density so as to minimize the amount of time spent in areas without ash. Once an ash tree was identified, the tree was tagged with orange flagging tape (Figure 2.2 c, d). Species, diameter at breast height (DBH), and crown class (dominant, co-dominant, intermediate, or overtopped) were recorded for each tree. Finally, GPS locations were recorded with a Trimble GEOxplorer 6000 and Zephyr external antenna (Sunnyvale, CA) to under 1-meter accuracy (approximately 100 GPS point fixes). GPS units increase accuracy by logging a number of position fixes at each point –sub meter accuracy can be achieved with as little as one point with a Trimble GPS (Bolstad et al. 2005), but in practice researchers will preferably log over 100 fixes per point (David Sandilands, *Pers. Comm*). GPS points were post corrected using Trimble Pathfinder Office software (Trimble, Germany).

A variable radius plot was established at each ash tree using a prism with a basal area factor of 15 ft^2/ac to determine co-occurring species, resulting in plots with radii between 3.5 m and 27 m (dependent on the DBH of the target tree). For all "in" trees that reached the canopy, we recorded tree species, DBH, crown class, and GPS point logged. Site 2 (13.5 ha) was sampled in an identical method, with preliminary surveys laying the groundwork for targeted sampling.

In addition, a subset of trees of all species were selected to have their crown area estimated by measuring the distance from the tree bole to the edge of the crown in each of the cardinal directions (N, E, S, W) and utilizing the quadratic mean crown width (MCW) equation:

$$\text{MCW}=2*\sqrt{((r_1^2 + r_2^2 + r_3^2 + r_4^2)/4)} \quad (1)$$

where r_1 through r_4 represent the crown radii, to provide an unbiased estimate of crown area (Russell and Weiskittel 2011).

Field data were summarized by tree species and total number of trees per species sampled, as well as classes used for further analysis (Table 2.1). Due to the small and often overlapping crowns, delineation presented significant difficulties and every effort was made to only delineate positively identified trees, leading to smaller than expected sample sizes and necessitating the grouping of species into classes. Species were grouped into classes by spectral similarity, thus sample size and class totals reflect those trees that were successfully identified and delineated.

Table 2.1 Field data summarizing tree species collected for training and model validation (left) and aggregated classes and number of samples used for classification (right) for G-LiHT data

Species	Species Class	Species Totals
Quaking aspen	Quaking Aspen	25
Balsam fir	Softwood	60
Black ash	Ash	83
Green ash	Ash	25
Eastern hemlock	Softwood	24
Northern white cedar	Softwood	42
Oak spp.	Other Hardwood	4
Other Hardwoods	Other Hardwood	6
Paper birch	Hardwood	12
Red maple	Red Maple	76
Red spruce	Softwood	17
White ash	Ash	21
White pine	Softwood	10
Yellow birch	Other Hardwood	18
Total		420

Class	Sample Totals
Ash (AS)	40
Quaking aspen (QA)	25
Other Hardwood (HW)	25
Red maple (RM)	38
Softwood (SW)	35

2.2.2. Remote sensing data and data pre-processing

We first present the overall workflow of this chapter (Figure 2.3). In this study we utilized hyperspectral data from NASA's G-LiHT airborne system collected in August 2017 with

1.5 nm spectral and 0.6 m spatial resolutions (Cook et al. 2013) in up to 185 spectral bands with 400-1000 nm spectral range, along with RGB orthomosaic data at 0.04 m spatial resolution.

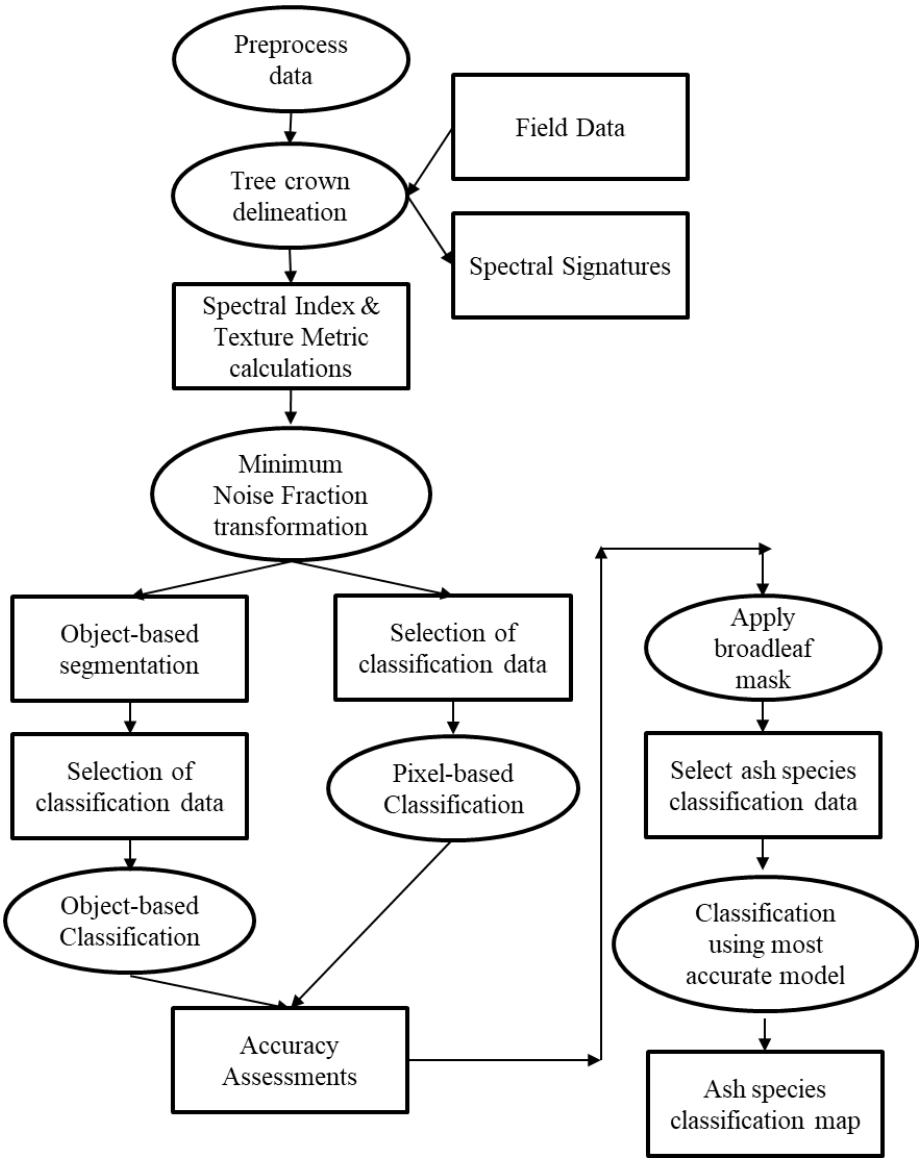

Figure 2.3 Workflow for development of ash tree species maps using G-LiHT hyperspectral data

G-LiHT data were orthorectified and atmospherically corrected using Fast Line-of-site Atmospheric Analysis of Spectral Hypercubes (FLAASH) (Cooley et al. 2002). All pre-processing was completed using ENVI version 5.5.2. First, the individual study sites were

clipped from the larger rasters before the spectral bands were inspected for noise. Bands that were visually identified as noisy were removed (22 bands), leaving 163 bands total. Based on the resulting hyperspectral data, a suite of SVIs and texture metrics were calculated (Table 2.2, Table 2.3). SVIs were selected based on previous research by Maschler et al. (2018); Pontius et al. (2017); Rahimzadeh-Bajgiran et al. (2018) to include a range of structural and physiological properties. Inter- and intra-crown texture metrics (such as homogeneity or variance), were also included, which other researchers have used along with spectral data to increase accuracy of models (Franklin et al. 2000). Kim et al. (2009) found that the ability to distinguish forest types was significantly increased when they incorporated grey-level co-occurrence metrics (a type of texture analysis) into their model. The resultant texture metrics, spectral indices, and spectral bands were combined, resulting in a 222 band data stack. This stacked image underwent Minimum Noise Fraction (MNF) transformation, which reprojects hyperspectral data onto orthogonal vectors that account for decreasing amounts of spectral variability before segregating noise from data, thereby reducing both the dimensionality and noise present in the data (Boardman and Kruse 2011; Pontius et al. 2017). By including SVIs and texture metrics in the data set to be reduced, of the resultant MNF bands, the top 40 most important bands were selected with a goal of preserving 15% of bands in the final analysis. The 40 MNF bands were visually inspected for noise and 2 bands were removed, leaving 38 (17%) of the 222 band data stack for classification and analysis.

Table 2.2 SVIs derived from G-LiHT hyperspectral data

Name	Equation	Reference
2-EVI^{S}	$2.5 * (\frac{B867 - B648}{B867 + (2.4 * B648)})$	Jiang et al. (2008)
ARI1^{P}	$(\frac{1}{B550}) - (\frac{1}{B700})$	Gitelson et al. (2001)
ARI2^{P}	$B800 * [(\frac{1}{B550}) - (\frac{1}{B700})]$	Gitelson et al. (2001)
ARVI^{P}	$\frac{B800 - (B650 - \gamma(B450 - B680))}{B800 + (B650 - \gamma(B450 - B680))}$	Kaufman and Tanre (1992)
BR^{S}	$(\frac{B663}{B481}) * (\frac{B547}{B481}) * (\frac{B722}{B481}) * (\frac{B831}{B481})$	Maschler et al. (2018); Waser et al. (2014)
CRI1^{P}	$(\frac{1}{B510}) - (\frac{1}{B550})$	Merzlyak et al. (2003)
CRI2^{P}	$(\frac{1}{B510}) - (\frac{1}{B700})$	Merzlyak et al. (2003)
DDVI^{P}	$(2 * B947 - B750) - (B648 - B546)$	Maschler et al. (2018)
DI^{P}	$(B722.84 - B663.54)$	Tucker (1979)
EVI^{S}	$2.5 * (\frac{B867 - B648}{B867 + (6 * B648) - (7.5 * B466) + 1})$	Liu and Huete (1995)
GARVI^{P}	$\frac{B750 - (B546 - (B466 - B670))}{B750 + (B546 - (B466 - B670))}$	Gitelson et al. (1996a)
GNDVI^{P}	$\frac{B750 - B546}{B750 + B546}$	Gitelson and Merzlyak (1998)
GR^{S}	$\frac{B546}{B663}$	Maschler et al. (2018); Waser et al. (2014)
GRDI^{P}	$\frac{B561 - B663}{B561 + B663}$	Tucker (1979)
GRR^{P}	$\frac{B546}{B663}$	Gitelson et al. (1996b)
IPVI^{P}	$\frac{B801.99}{B801 + B678}$	Crippen (1990)

Table 2.2 Continued

MCARI[P]	$((B700 - B670) - 0.2(B700 - B550)) * \left(\frac{B700}{B670}\right)$	Daughtry et al. (2000)
MCARII[P]	$\frac{1.5\left(2.5(B800 - B670) - 2.5(B670 - B550)\right)}{\sqrt{(2B800 + 1)^2 - (6B800 - 5\sqrt{B670} - 0.5}}$	Haboudane et al. (2004)
MNDI[P]	$\frac{B750 - B707}{B750 + B707 - (2 * B444)}$	Sims and Gamon (2002)
mRENDVI[P]	$\frac{B750 - B705}{B750 + B705 - (2 * B445)}$	Sims and Gamon (2002)
mRESR[P]	(B750-B445)/(B705-B445)	Sims and Gamon (2002)
mSR[P]	$\frac{B750 - B444}{B707 - B444}$	Sims and Gamon (2002)
mTVI[S]	$1.2 * \left(1.2 * (B800 - B550) - 2.5 * (B670 - B550)\right)$	Haboudane et al. (2004)
mTVII[S]	$\frac{1.5\left(1.2(B800 - B550) - 2.5(B670 - B550)\right)}{\sqrt{(2B800 + 1)^2 - (6B800 - 5\sqrt{B670} - 0.5}}$	Haboudane et al. (2004)
NDVI[S]	$\frac{B801 - B678}{B801 + B678}$	Rouse et al. (1974)
NDREI[P]	$\frac{B787 - B721}{B787 + B721}$	Barnes et al. (2000)
OSAVI[S]	$\frac{(1 + 0.16)(B800 - B670)}{B800 + B670 + 0.16}$	Rondeaux et al. (1996); Wu et al. (2008)
PRI[P]	$\frac{B531 - B570}{B531 + B570}$	Gamon et al. (1997) Penuelas et al. (1995)
PSRI[P]	$\frac{B678 - B503}{B750}$	Merzlyak et al. (1999)
RVI[S]	$\frac{B802}{B678}$	Jordan (1969)

Table 2.2 Continued

RENDVI[P]	$\frac{B750 - B707}{B750 + B707}$	Gitelson and Merzlyak (1994); Sims and Gamon (2002)
RR[S]	$(\frac{B831}{B663}) * (\frac{B546}{B663}) * (\frac{B831}{B721})$	Maschler et al. (2018); Waser et al. (2014)
SIPI[P]	$\frac{B800 - B445}{B800 - B680}$	Penuelas et al. (1995)
TVI[S]	$\frac{[120 * (B750 - B550) - 200 * (B670 - B650)]}{2}$	Broge and Leblanc (2001)
VARI[P]	$\frac{B561 - B663}{B561 + B663 - B488}$	Gitelson et al. (2002)
VREI1[P]	$\frac{B740}{B720}$	Vogelmann et al. (1993)

2-EVI: 2-band Enhanced Vegetation Index, ARI1: Anthocyanin Reflectance Index 1, ARI2: Anthocyanin Reflectance Index 2, ARVI: Atmospherically Resistant Vegetation Index, BR: Blue Ratio, CRI1: Carotenoid Reflectance Index 1, CRI2: Carotenoid Reflectance Index 2, DDVI: Difference Difference Vegetation Index, DI: Difference Index, EVI: Enhanced Vegetation Index, GARVI: Green Atmospherically Resistant Vegetation Index, GNDVI: Green Normalized Difference Vegetation Index, GR: Green Ratio, GRDI: Green-Red Difference Index, GRR: Green-Red Ratio, IPVI: Infrared Percentage Vegetation Index, mCARI: Modified Chlorophyll Absorption Ratio Index, mCARII: Modified Chlorophyll Absorption Ratio Index – Improved, mNDI: Modified Normalized Difference Index, mRENDVI: Modified Red Edge Normalized Difference Vegetation Index, mRESR: Modified Red-Edge Simple Ratio, mSR: Modified Simple Ratio, mTVI: Modified Triangular Vegetation Index. mTVII: Modified Triangular Vegetation Index – Improved, NDVI: Normalized Difference Vegetation Index, NDREI: Normalized Difference Red-Edge Index, OSAVI: Optimized Soil Adjusted Vegetation Index, PRI: Photochemical Reflectance Index, PSRI: Plant Senescence Reflectance Index, RVI: Ratio Vegetation Index, RENDVI: Red-Edge Normalized Difference Vegetation Index, RR: Red Ratio, SIPI: Structure Insensitive Pigment Index, TVI: Triangular Vegetation Index, VARI: Visible Atmospherically Resistant Index, VREI1: Vogelmann Red-Edge Index 1.

[P] The index measures physiological traits such as pigment or chlorophyll concentrations.

[S] The index measures structural/physical traits such as leaf area index (LAI).

Table 2.3 Texture metrics used for tree genera classification

Texture Metric	Equation	Reference
1st Order Data Range (700 nm & 847 nm)	$Max - min$	Anys et al. (1994)
1st Order Mean (700 nm & 847 nm)	$\sum_{i=0}^{N_g-1} iP(i)$	Anys et al. (1994)
1st Order Variance (700 nm & 847 nm)	$\sum_{i=0}^{N_g-1} (i-M)^2 P(i)$	Anys et al. (1994)
1st Order Entropy (700 nm & 847 nm)	$\sum_{i=0}^{N_g-1} P(i) * lnP(i)$	Anys et al. (1994)
2nd Order Mean (700 nm & 847 nm)	$\sum_{i=1}^{N_g}\sum_{j=1}^{N_g} i * P(i,j)$	Haralick et al. (1973)
2nd Order Variance (700 nm & 847 nm)	$\sum_{i=1}^{N_g}\sum_{j=1}^{N_g}(i-\mu)^2 P(i,j)$	Haralick et al. (1973)
2nd Order Homogeneity (700 nm & 847 nm)	$\sum_{i=1}^{N_g}\sum_{j=1}^{N_g}\frac{1}{1+(i-j)^2}P(i,j)$	Haralick et al. (1973)
2nd Order Contrast (700 nm & 847 nm)	$\sum_{i=1}^{N_g}\sum_{j=1}^{N_g} P(i,j)(i-j)^2$	Haralick et al. (1973)
2nd Order Dissimilarity (700 nm & 847 nm)	$\sum_{i=1}^{N_g}\sum_{j=1}^{N_g} P(i,j)\lvert i-j\rvert$	Haralick et al. (1973)
2nd Order Entropy (700 nm & 847 nm)	$\sum_{i=1}^{N_g}\sum_{j=1}^{N_g} P(i,j)\log(P(i,j))$	Haralick et al. (1973)
2nd Order Second Moment (700 nm & 847 nm)	$\sum_{i=1}^{N_g}\sum_{j=1}^{N_g}\{P(i,j)\}^2$	Haralick et al. (1973)
2nd Order Correlation (700 nm & 847 nm)	$\frac{\sum_{i=1}^{N_g}\sum_{j=1}^{N_g}(ij)P(i,j)-\mu_x\mu_y}{\sigma_x\sigma_y}$	Haralick et al. (1973)

where P(i) = probability of each pixel value; N_g = number of distinct grey levels in the quantized image; i and j = the row and column numbers in the spatial matrix; p(i,j) = the value of cell i,j in the matrix; μ = the mean; and σ = the standard deviation.

2.2.3. Pixel-based classification methods

Individual tree crowns were identified with the help of the GPS points collected in the field using ENVI 5.5.2. Due to the condensed and overlapping nature of many of the tree canopies in the study area, only trees in the Dominant, Co-Dominant, or Intermediate crown classes were considered and extreme care was taken to ensure accurate attribution. Trees were classed into groups (see Table 2.1), with the ash species grouped together only for the initial classification. Individual tree crowns were identified and delineated using the true-color hyperspectral image. These crowns were used to create spectral signatures for each target species group and to extract mean values from the MNF-reduced hyperspectral data for classification purposes.

2.2.4. Object-based classification methods

In object-based analysis, algorithms are applied to a stack of input variables to group pixels into objects based on similarities in the input variables, which then serve as the basis for classification. In this case, the 38 bands resulting from the MNF transformation were used as the input for segmentation. Segmentation was performed using L3Harris GeoSpatial's ENVI 5.5.2 Feature Extraction module and the Edge segmentation method. ENVI-Edge utilizes a patented method invented by Jin (2012) that computes a gradient map from an image, computes a modified gradient image via scale level, and then uses a Sobel edge detection method to identify boundaries between objects. If the results are satisfactory, then a watershed transformation based on the modified gradient map is applied to the whole image, resulting in segmentation objects.

ENVI provides two main methods for adjusting the output of the segmentation – scale and merge parameters. In the Edge segmentation method, the scale parameter eliminates the stated percentage of lowest intensity gradients while the merge parameter will combine adjacent

segments (based on spectral and spatial information) with a merging cost less than the defined parameter (Jin 2012). Watershed segmentations often result in over-segmentation of the desired tree crowns (Yang et al. 2015; Yang et al. 2014b), so finding a suitable merge parameter is highly advantageous. The determination of such parameters is largely done experimentally (Amini et al. 2018; Garzon-Lopez and Lasso 2020; Pontius et al. 2017) and the same was attempted in this study. Scale 10 was determined to adequately segment crowns and other objects, however a suitable merge factor was unable to be found, likely due to the large differences in the sizes of tree crowns of target species in the study area. As such, no merge was performed.

Training data were selected for each species class utilizing the GPS points collected in the field (Table 2.1) and the delineated tree crowns identified previously.

2.2.5. Classification modeling

Once all input variables were prepared for pixel-based and object-based approaches, we implemented classification (Blaschke and Hay 2001) using RF and SVM in RStudio (Team 2015), an open-source UI for the R Statistical Programming Language (Shruthi et al. 2014)R version 4.0.3 (R Core Team 2020).

SVM is a non-parametric supervised machine learning algorithm that uses training data to construct hyperplanes in a multidimensional feature space that maximizes differences within the data classes, corresponding to a kernel function (Ferreira et al. 2019; Noble 2006; Zoleikani et al. 2017). While some researchers have found that the radial kernel function provides better classification results (Amini et al. 2018), the polynomial kernel function produced better results in initial classifications and, as such, was used in this study.

RF is also a non-parametric method based on a combination of decision tree predictors (Breiman 2001) that has been used for numerous applications such as defoliation detection (Bhattarai et al. 2020), tree identification (Sapkota and Liang 2020), and land cover mapping (Wang et al. 2018). This algorithm is well suited to hyperspectral imagery because of its ability to handle a large number of variables (Amini et al. 2018; Immitzer et al. 2012).

Each classification data set was split randomly into 60% training data and 40% testing data and each model was trained using 10-fold repeated cross validation.

A set of statistical measures were calculated for each algorithm, namely mean kappa, mean accuracy, out-of-bag error (for RF), and confusion matrices. Based on these statistics the most accurate classification method was selected and utilized in black ash identification.

2.2.6. Black ash classification

Once we derived a suitably accurate model for species level identification, we moved to differentiating black ash within the ash genus. In order to separate out black ash, we first created a mask of only those pixels representing broadleaf tree crowns, as determined by the initial round of classification (AS, QA, RM, HW). After determining that SVM object-based methods created the most realistic ash genus classification map, training data for each ash species were selected. Due to sample size constraints and spectral similarity, green and white ash were grouped together (Table 2.4). Classification proceeded in a nearly identical fashion to the first round (Section 2.2.4) with broadleaf and ash classes. Due to spectral similarity and concerns about class size, we combined the green and white ash, RM, and HW classes, with 30% of each species randomly selected to balance both internal class species distribution and the total with other (BA

and QA) classes. In addition, 50% of the data was reserved for testing purposes (as opposed to 40% in the initial round) due to concern about having adequate external validation samples.

Table 2.4 Black ash classification classes and total number of samples

Class	Sample Totals
Black ash (BA)	21
Quaking aspen (QA)	25
Red maple, green and white ash, and other hardwood (HW)	25

2.3. Results

2.3.1. Evaluation of spectral bands for ash classification

Spectral signatures for all classes were calculated (Figure 2.4) using the de-noised G-LiHT hyperspectral data, using the same training data used for the pixel-based classification.

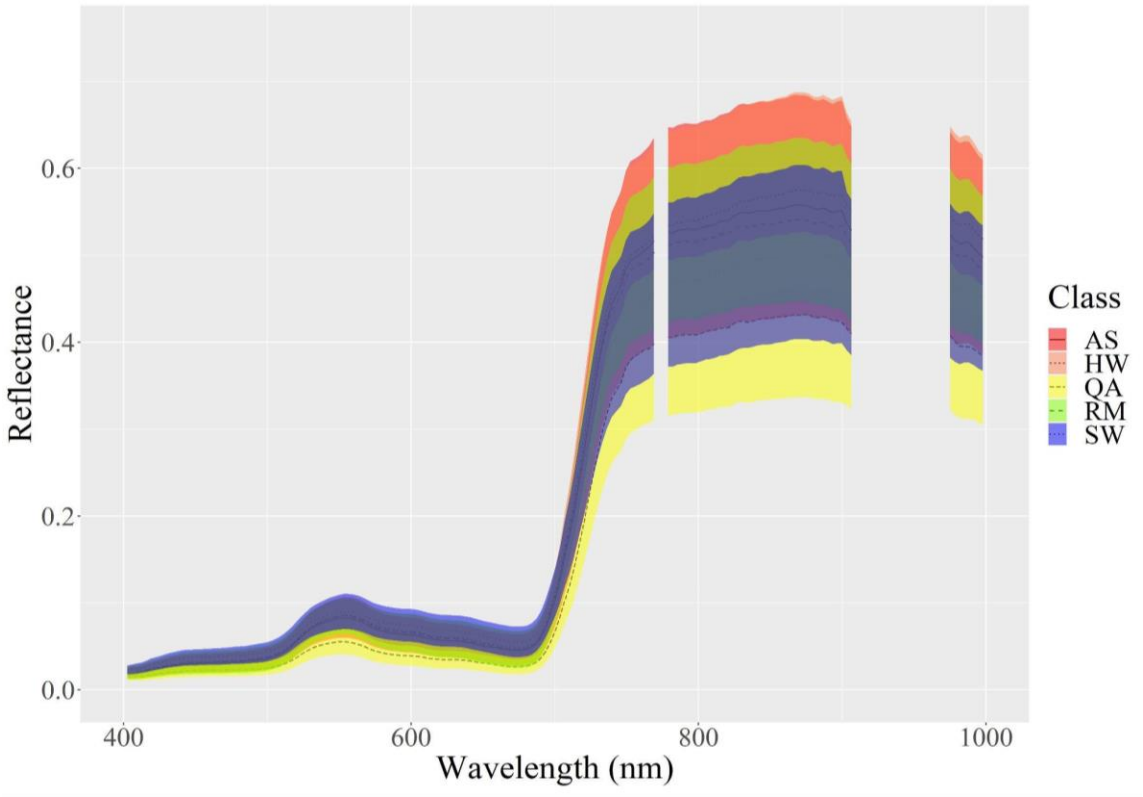

Figure 2.4 Mean spectral signatures of ash and co-occurring genera and species, derived from G-LiHT hyperspectral data. Shaded area equates to Mean +/- Standard Deviation. AS = ash, HW = other hardwood, QA = quaking aspen, RM = red maple, SW = softwood

The statistical significance of each wavelength between pairs of classes was calculated (Figure 2.5). Ash (AS) shows significant separation from softwood (SW) and quaking aspen (QA) over most of the visible spectrum (400-750 nm), but is not significantly different from either red maple (RM) or the mixed hardwood classes. Given the similarity over the optical spectrum, different sources of data (such as texture metrics) needed to be included to achieve suitable differentiation.

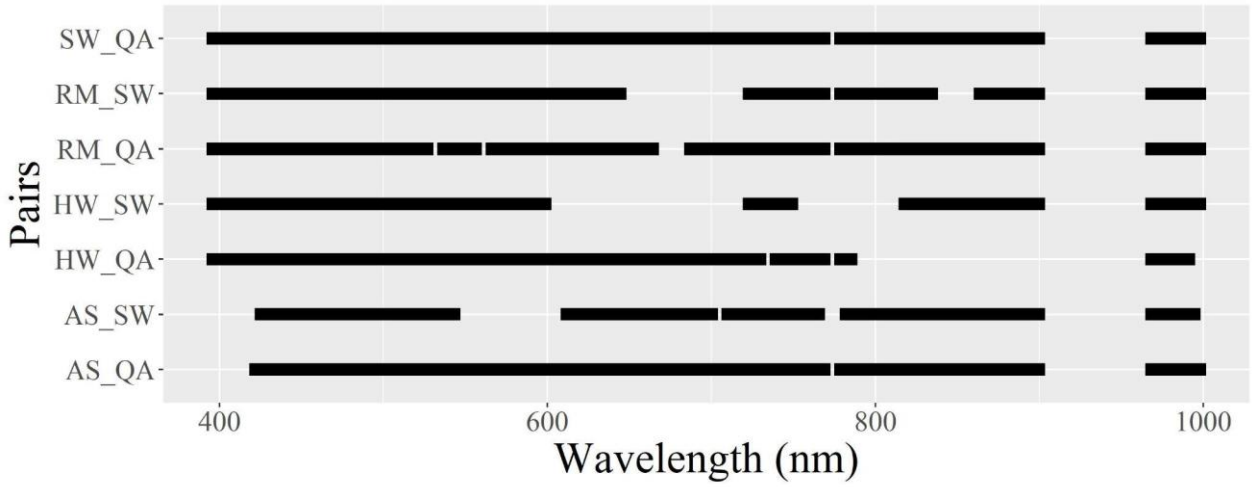

Figure 2.5 Significance of spectral signature difference between ash and co-occurring genera. Solid black lines indicate statistically significant differences between class pairs (P<0.05). AS = ash, HW = other hardwood, QA = quaking aspen, RM = red maple, SW = softwood. Note - no statistically different wavelength pairs for AS, HW, and RM classes were observed.

2.3.2. Segmentation results

Multiple segmentation scales were utilized to determine the best scale for individual tree delineation. Scale 5 (Figure 2.6a) shows over-segmentation even on small crowns, while scale 20 (Figure 2.6c) shows significant under-segmentation. Scale 10 (Figure 2.6b) did over-segment large crowns, however this was expected (Yang et al. 2015) and scale 10 showed the greatest ability to identify individual crowns while not producing an overwhelming amount of over-segmentation.

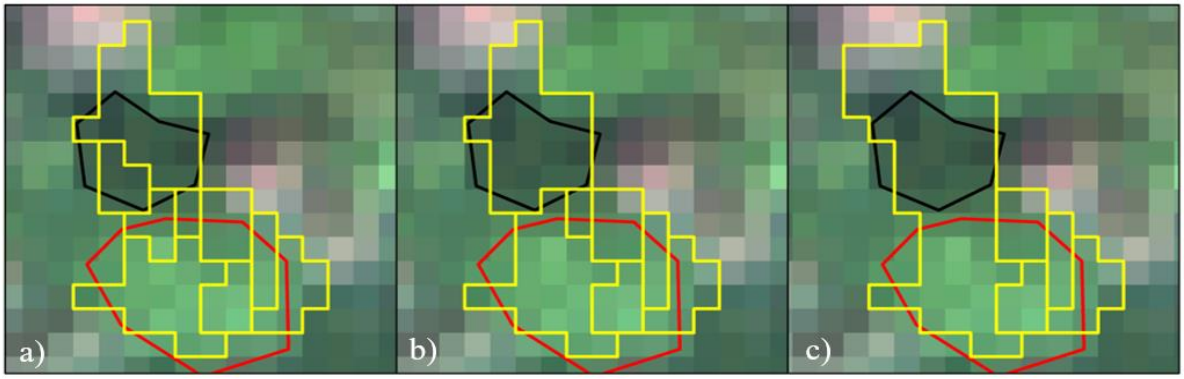

Figure 2.6 Comparison of segmentation scale factors, red = ash tree crown, black = gap in canopy

2.3.3. Ash species classification

With all areas that were identified as belonging to the SW class removed from the image, spectral signatures for each broadleaf class were calculated (Figure 2.7) using the de-noised G-LiHT hyperspectral data, using the same training data polygons as for the pixel-based classification. For this round of classification, green and white ash were separated into a distinct class (AS) from black ash (BA) and the SW class was excluded. There is clear differentiation between BA and AS in the 800-900nm range and in the 970-1000nm range.

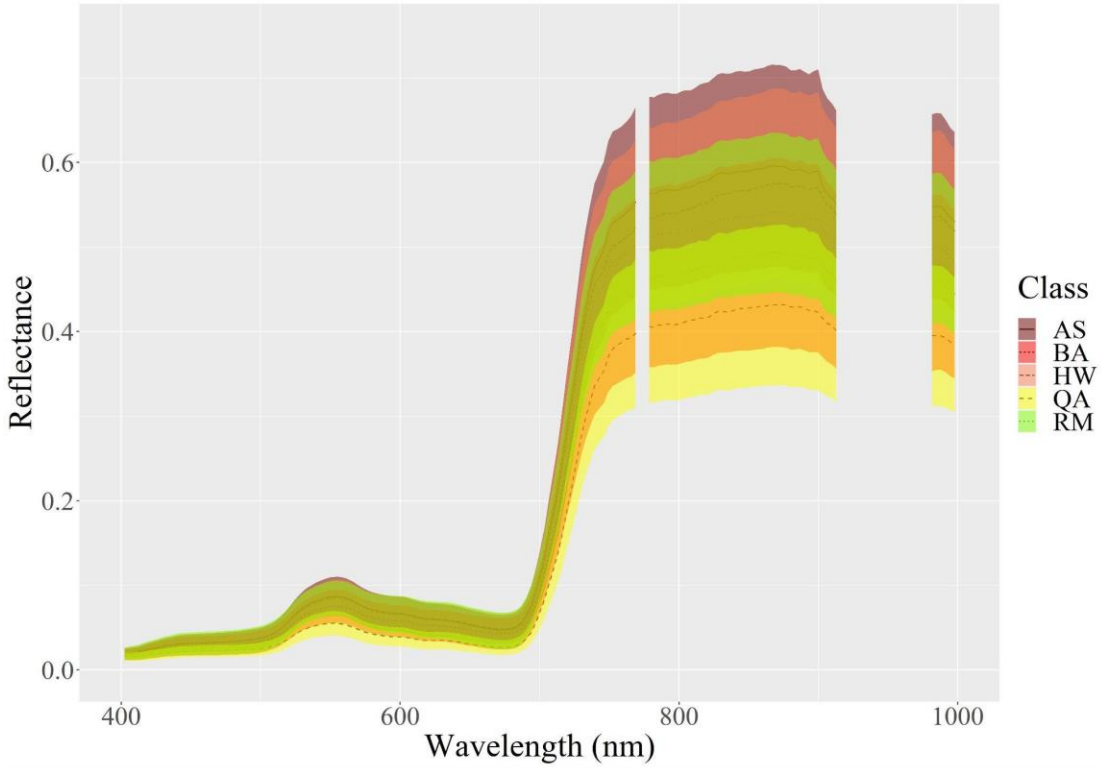

Figure 2.7 Mean spectral signatures of different species of ash and co-occurring species groups derived from G-LiHT hyperspectral data. Shaded area equates to Mean +/- Standard Deviation. AS = green and white ash, BA = black ash, HW = other hardwood, QA = quaking aspen

Statistical analysis of the spectral band pairs reveals key significant differences between species (Figure 2.8). While the ash (AS), red maple (RM), and hardwood (HW) classes were found to not be significantly different from each other, black ash (BA) was able to be differentiated. In particular, the red-edge and near infrared portions of the spectrum (730-1000nm) provide for significant differences between black ash (BA) and all co-occuring species. Quaking aspen (QA) was found to be significantly different from all other classes.

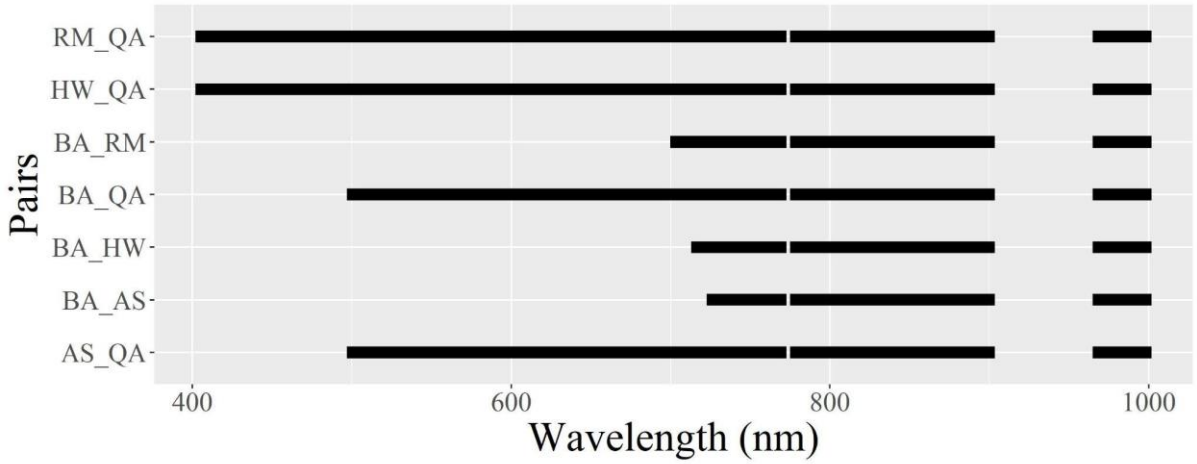

Figure 2.8 Significance of spectral signature difference between different species of ash and co-occurring species groups. Solid black lines indicate statistically significant differences between class pairs (P<0.05). Note – no significant spectral bands for AS_HW

2.3.4. Genera classification results, model evaluation and map production

Confusion matrices and accuracy metrics of pixel-based classification were developed (Table 2.5). The overall accuracy and kappa coefficient of the pixel-based RF model were 64.1 % and 0.54, respectively. While the AS class was slightly confused with the RM and HW classes, generally it was separated from other classes.

The overall accuracy and kappa coefficient of the pixel-based SVM model were 67.2 % and 0.58, respectively. Similar to RF, the AS class was slightly confused with the RM and HW classes but generally was separable. The mean and standard deviation of the pixel-based method were also calculated (Table 2.6).

Confusion matrices and accuracy metrics of object-based classification methods were developed (Table 2.7). The overall accuracy and kappa coefficient of the object-based RF and object-based SVM models were 64.1% and 0.54 and 64.19 % and 0.654 respectively. Using object-based classification the AS class was again slightly confused with the RM and HW classes. The object-based classification method generally outperformed the pixel-based method. Between classification algorithms, SVM outperformed RF where SVM yielded overall accuracies over 70% regardless of classification method. The mean and standard deviation of the object-based method were also calculated (Table 2.8).

Table 2.5 Confusion matrices and accuracy metrics of G-LiHT pixel-based classification methods for ash genus classification. PA = Producer's Accuracy, UA = User's Accuracy

Model	Species	AS	HW	QA	RM	SW	UA (%)
Pixel + RF	AS	9	2	0	5	1	52.9
	HW	0	3	0	1	0	75.0
	QA	0	0	9	0	1	90.9
	RM	3	3	0	9	1	56.2
	SW	3	2	1	0	11	64.7
	Total	15	10	10	15	14	
	PA (%)	60.0	30.0	90.0	60.0	78.6	
Overall accuracy **64.1%** and kappa coefficient 0.54							
Pixel + SVM	AS	11	3	0	4	0	61.1
	HW	2	1	0	2	0	20.0
	QA	0	0	9	0	0	100
	RM	2	2	0	9	1	64.3
	SW	0	4	1	0	13	72.2
	Total	15	10	10	15	14	
	PA (%)	73.3	10.0	90.0	60.0	92.9	
Overall accuracy **67.2%** and kappa coefficient 0.58							

Table 2.6 Internally-derived accuracy metrics (Mean ± Standard Deviation) of G-LiHT pixel-based methods for ash genus classification.

Model	Accuracy (%)	kappa	Out-of-bag error (%)
Pixel + RF	72.1 ± 13.8	0.64 ± 0.17	28.6
Pixel + SVM	72.4 ± 13.7	0.65 ± 0.17	

Table 2.7 Confusion matrices and accuracy metrics of G-LiHT object-based classification methods for ash genus classification. PA = Producer's Accuracy, UA = User's Accuracy

Model	Species	AS	HW	QA	RM	SW	UA (%)
Object + RF	AS	9	2	0	8	0	47.4
	HW	1	2	0	0	0	66.7
	QA	0	1	10	0	0	90.9
	RM	5	3	0	6	0	42.9
	SW	0	2	0	1	14	82.4
	Total	15	10	10	15	14	
	PA (%)	60.0	20.0	100.0	40.0	100.0	
Overall accuracy **64.1%** and kappa coefficient 0.54							
Object + SVM	AS	10	4	0	8	0	45.5
	HW	0	1	0	0	0	100.0
	QA	0	1	10	0	0	90.9
	RM	5	2	0	6	0	46.2
	SW	0	2	0	1	14	82.4
	Total	15	10	10	15	14	
	PA (%)	66.7	10.0	100.0	40.0	100.0	
Overall accuracy **64.1%** and kappa coefficient 0.54							

Table 2.8 Internally-derived accuracy metrics (Mean ± Standard Deviation) of G-LiHT object-based methods for ash genus classification

Model	Accuracy (%)	kappa	Out-of-bag error (%)
Object + RF	73.7 ± 11.5	0.66 ± 0.15	25.5
Object + SVM	79.5 ± 13.9	0.74 ± 0.18	N/A

The distribution of internal accuracies derived from each model and the statistical significance of those accuracies were calculated (Figure 2.9). The object-based SVM classification had the highest overall accuracy and, while the pixel-based SVM model was not significantly better than the pixel-based RF model, the pixel-based SVM model was chosen for consistency. The classification maps of the best object-based and pixel-based methods (SVM) with subsets comparing RF- and SVM-derived maps were then developed (Figure 2.10 and 2.11).

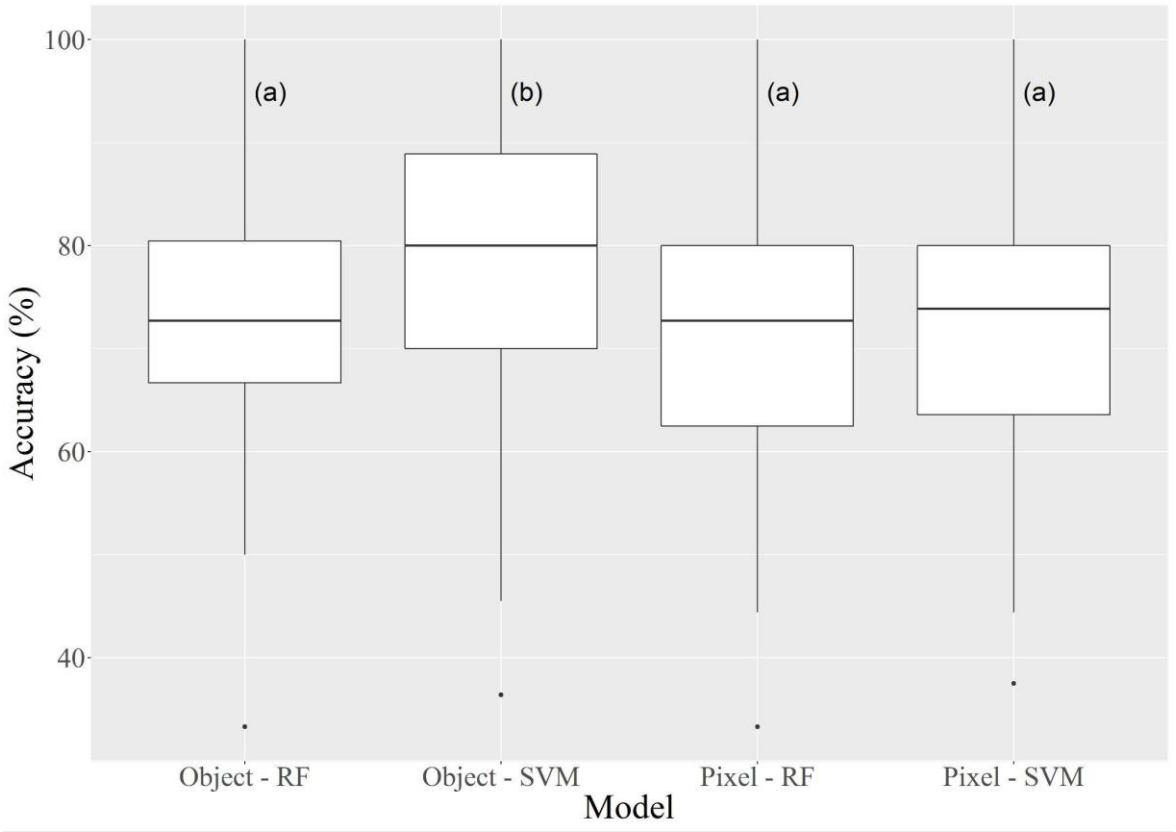

Figure 2.9 Distribution of G-LiHT based model accuracies derived from internal 10-fold cross-validation. Letter pairs indicate statistical similarity based on $p<0.05$.

In terms of internal validation, both pixel-based methods achieved nearly identical overall accuracies and kappa values (Table 2.5). In addition, the object-based RF model, while achieving a slightly higher overall accuracy than the pixel-based methods, produced a statistically similar overall accuracy. The object-based SVM model, however, produced a statistically higher mean accuracy than the other models (Figure 2.9). While the object-based SVM model does not produce the highest Producer's or User's Accuracy of ash (pixel-based SVM model is the highest in both), it does produce the highest Overall Accuracy by a statistically significant margin.

Ash and co-occurring genera were successfully identified in both study sites using all four classification approaches (Figure 2.10 and Figure 2.11). Each model presents a similar pattern - there is some disagreement between hardwood classes (AS, RM, HW), but general

consistency in the softwood (SW) class. Confidence in the models are increased by the relative abundances of QA and SW in Sites 1 and 2, respectively – Site 1 had significant amounts of aspen but fewer softwood species, while Site 2 had significant amounts of softwood species but little to no aspen. In addition, AS is consistently predicted in areas that align with ash's ecological needs, such as along stream beds, roads, and in wetlands, further increasing confidence in the overall classification approach. This is particularly evident in Site 2, where both the object- and pixel-based SVM models predict relatively lower amounts of RM in the northern portion of the stand that is slightly drier and more conducive to other hardwood species, but as one moves south in the site (and the site becomes wetter) higher levels of RM and AS (compared to HW) are predicted.

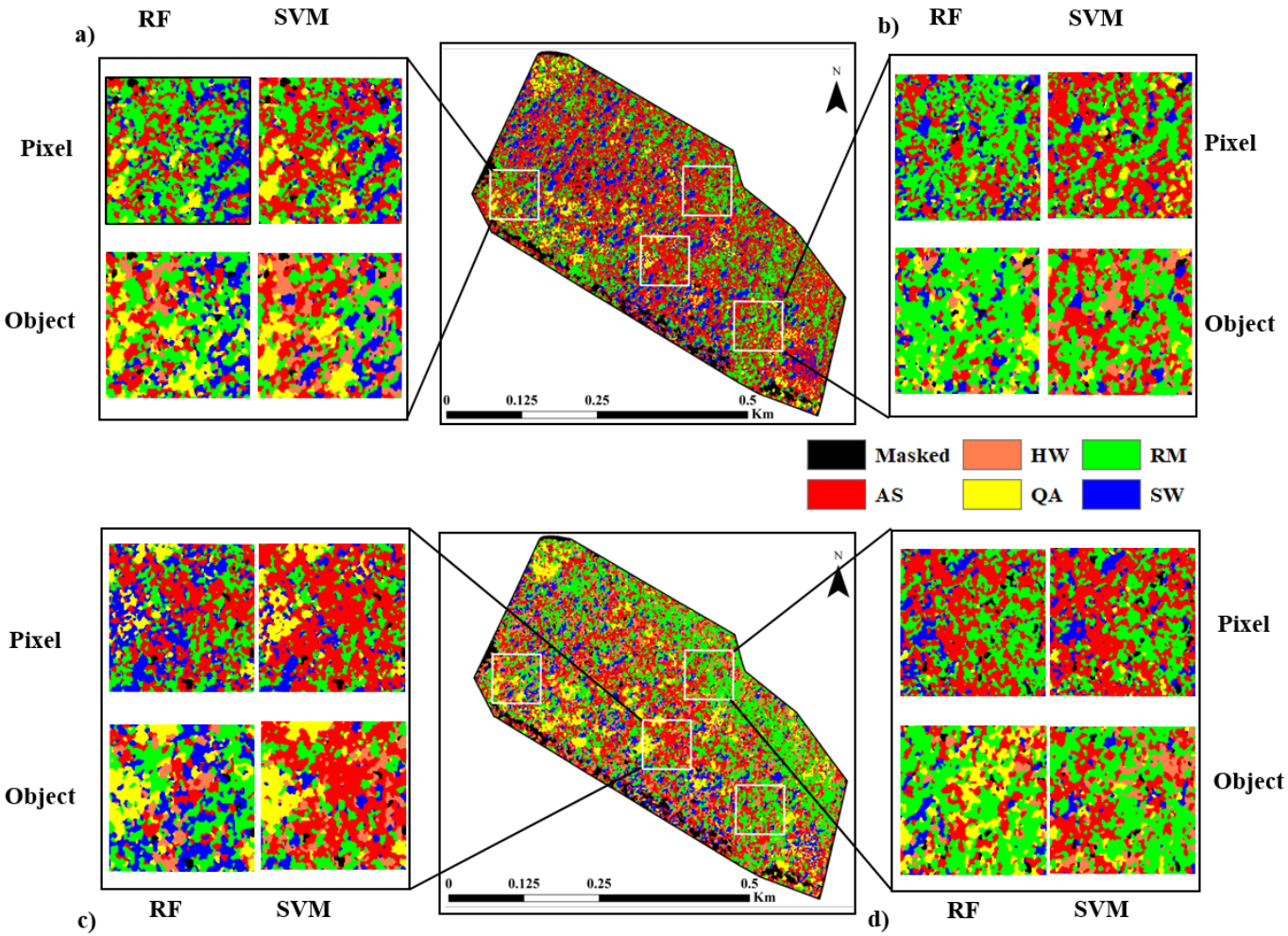

Figure 2.10 Classification map of Site 1 using G-LiHT hyperspectral data and varied classification methods. Top = pixel-based SVM, Bottom = object-based SVM. AS = ash, HW = hardwood, QA = quaking aspen, RM = red maple, SW = softwood. Focus areas were chosen to highlight different aspects of model:
a) Consistency in SW but inconsistency in AS/RM/HW classes b) swampy area dominated by RM, some mixed classification with AS c) over-prediction of AS in SVM-based approaches and confusion between RM and HW d) ridge with high levels of broadleaf trees, but high degree of instability in AS, HW, and RM classes

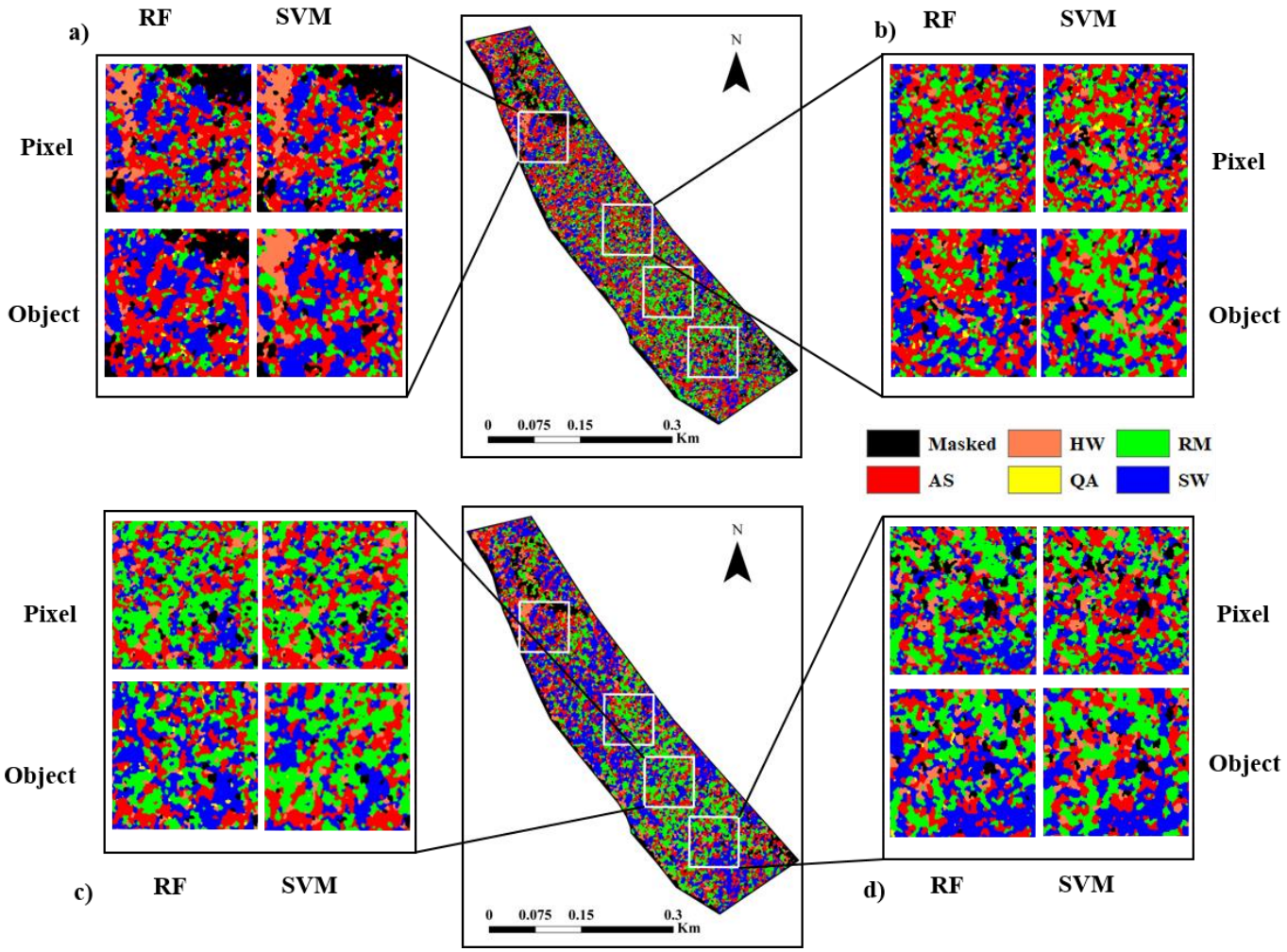

Figure 2.11 Classification map of Site 2 using G-LiHT hyperspectral data and varied classification methods. Top = pixel-based SVM, Bottom = object-based SVM. AS = ash, HW = hardwood, QA = quaking aspen, RM = red maple, SW = softwood. Focus areas were chosen to highlight different aspects of mode:

a) HW, RM, AS/SW classification mostly consistent, but SVM predicting higher levels of HW; b) SW area consistent, pixel-based methods identifying increased variation; c) consistency between pixel- and object- based models, with increased variation in pixel-based classification; and d) transition to upland SW dominated area in south, model picking up increased SW presence.

2.3.5. Black ash classification

Both the overall accuracy and kappa coefficient (Table 2.9 and 2.10) suggest that the model is having some success separating black ash from other hardwoods. There are some expected misclassifications between the BA and the HW classes, but nonetheless BA is classified with a Producer's and User's Accuracy of 70%. Generally speaking the model is over predicting black ash, especially in Site 1 along the northeastern border, but is highlighting concentrations of black ash successfully in the southwestern portion of Site 1 (Figure 2.12.a) and in the interior of Site 2 (Figure 2.12.b). With the exception of the northeastern ridge in Site 1, the model has predicted each ash species in its generally best habitat: black ash in wetlands and swamps, and green and white ash along streams and roadways and in well drained, moist soil along ridges and streams. This ecological consistency further suggests that the model is aligned with physical realities.

Table 2.9 Confusion matrix and accuracy metrics of black ash hyperspectral identification. PA = Producer's Accuracy, UA = User's Accuracy

Model	Species	BA	HW	QA	UA (%)
Object + SVM	BA	7	2	1	70.0
	HW	3	10	0	76.9
	QA	0	0	11	100
	Total	10	12	12	
	PA (%)	70.0	83.3	91.7	
Overall accuracy **82.4%** and kappa coefficient **0.73**					

Table 2.10 Internally-derived accuracy metrics (Mean ± Standard Deviation) of black ash identification

Model	Accuracy (%)	kappa
Object + SVM	77.1 ± 19.8	0.65 ± 0.29

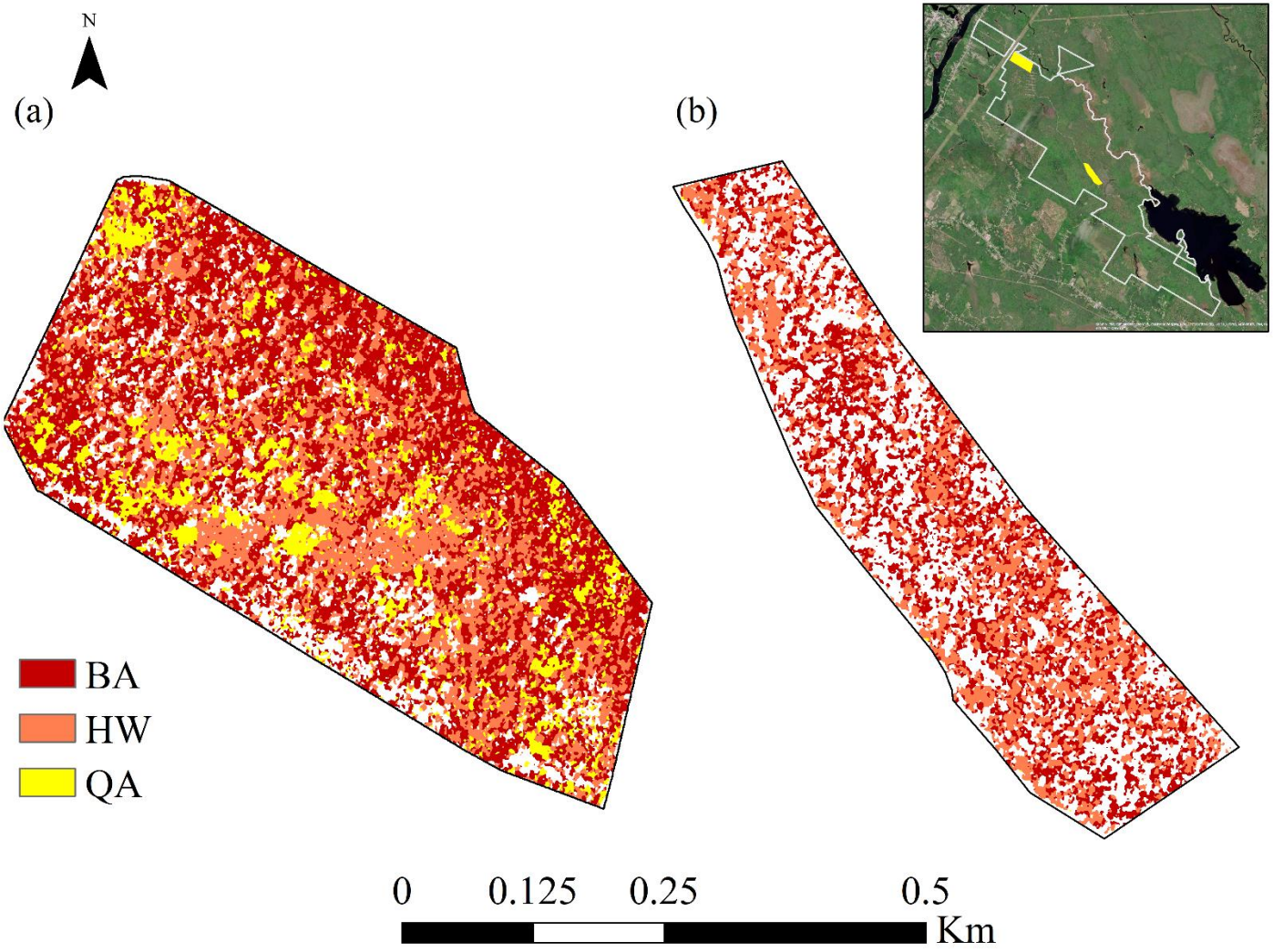

Figure 2.12 Black ash classification maps utilizing object-based, SVM algorithm of (a) Site 1 and (b) Site 2. (a) Note over prediction of black ash in ridge along northeastern border.

2.4. Discussion

2.4.1. Comparison of pixel- and object-based classifiers

Pixel- and object-based classification methods produced very similar results from a statistical point of view and the kappa values suggest the accuracy measures are not due to random chance. However, there are clear differences in classification maps, mostly centered on red maple, ash, and other hardwoods. As these discrepancies are not adequately captured via statistics a broader view must be taken into consideration. The HW class is dominated by white and paper birch, while the SW is mostly red spruce and balsam fir. Confusion between broadleaf classes – ash, maple, and mixed hardwood/birch – is similar to what other researchers have experienced (Lisein et al. 2015; Maschler et al. 2018). In our pixel-based methods there is some confusion between AS and SW, which primarily consists of white pine, eastern hemlock, red spruce, and balsam fir. While these species are not spectrally similar to ash, they co-occur with high frequency and with high density (Costanza 2015; Erdmann et al. 1987) and overtopped trees could have contributed to contamination of the hardwood (AS, RM, HW) classes.

Taking a step back to broadly assess the classification patterns, the pixel-based approaches generally result in over-classification of ash, especially in Site 1. With a few exceptions, ash trees in Maine tend to grow in a dispersed pattern, and in some instances ash will become established along a stream bank which can then be traced back to a single seed source. These patterns are apparent in both the object- and pixel-based classification approaches, however, pixel-based approaches tend to overestimate the overall abundance of ash, particularly in Site 1. It is possible this class confusion is due to the complex, overlapping nature of the tree canopy – the majority of areas with the highest class differences are also those areas that had the smallest average tree crown (J. Furniss, personal observation). In these areas even those trees

that reached the canopy would maintain very small crowns, many times overlapping other trees or presenting oddly shaped crowns. It is entirely possible that the suite of metrics calculated through the object segmentation process is better able to differentiate these small, overlapping crowns than pixel-based methods are able to.

Even in the face of class disagreements, the models produce useable results. All models were able to highlight potential areas of ash growth.. As the focus of this study is to identify individual ash trees, however, object-based methods seem to present the most viable path forward. Based on typical ash dispersal patterns in Maine, and researchers' own experience on the sites, it seems as though pixel-based approaches are identifying the possible range of ash within a given area while the object-based approaches are better at identifying individual crowns and accurately classifying them. As the goal is to find as much ash as possible to facilitate preservation, erring on the side of over-prediction may be preferred, but the ability to identify individual trees is paramount.

2.4.2 RF vs. SVM classification

Statistically, the RF and SVM pixel-based and RF object-based classification models performed similarly, while the SVM object-based model performed significantly better. While RF is versatile and can be applied to a wide variety of settings and data types, SVM has been shown to maintain high accuracy despite changes to sample size (Thanh Noi and Kappas 2018) and to outperform RF in a variety of settings, such as crop type classification (Nitze et al. 2012) and land cover classification (Thanh Noi and Kappas 2018). RF is a relatively straightforward decision tree approach (Breiman 2001), while SVM constructs hyperplanes to compare pairwise data points (Noble 2006), potentially allowing for SVM to capture a higher degree of differentiation between similar classes - as can be seen in the increased class variation of the

SVM-classified maps. Accordingly, however, SVM is significantly more computationally intensive and could present difficulties for large scale classification.

2.4.3. Comparisons to other work

These findings largely align with what other researchers have found. Maschler et al. (2018), for example, achieved nearly 92% overall accuracy, but only 72.7% Producer's Accuracy for ash - which compares well with the 66.7% (using object-based SVM method) achieved in this study. Critically, however, the models developed in this study are over predicting ash as evidenced by our 45.5% User's Accuracy, compared to 88.7% achieved by Maschler et al. (2018). This difference is likely in large part due to differences in sample size between the two studies, as Maschler et al. (2018) included 699 individual delineated crowns compared to 163 in this study. Pontius et al. (2017) achieved an overall accuracy of 81% in an urban environment, with an ash Producer's Accuracy of 45% and a User's Accuracy of 94% using 290 total samples. The increase in accuracy concurrent with sample size is expected and promising, given the limited sample size of this study. The scattered nature of ash, its non-dominance, and small crown sizes in our study sites might have also contributed to the lower accuracy of our models.

2.4.4. Black ash classification

Utilizing object-based methods and SVM, black ash was successfully differentiated from white and green ash. Ash species are known to hybridize with each other when present at the same location, with DNA sequencing sometimes the only way to tell one species from another (Wallander 2008). As such, it is not surprising that there was some mixing between the black ash and hardwood-maple-ash class. Generally speaking, the classification results correspond to the physical characteristics of the landscape, with black ash in lower lying, swampy areas, such as

the southern portion of Site 2 (Figure 2.12.b) and the western and eastern portions of Site 1 (Figure 2.12.a). Critically for the identification of ash in Maine, this method detected not only larger areas of ash, like along a stream in the central portion of Site 1 (Figure 2.12, a) or the large green ash along the western border of Site 2 (Figure 2.12, b), but also smaller black ash crowns intermixed with other species as seen especially in the southern portion of Site 2 (Figure 2.12, b). The northeastern ridge in Site 1, however, remains a concern due to the over prediction of black ash and a reason for further refinement of the model.

2.5. Conclusions

We were able to differentiate ash from other co-occurring genera, and then differentiate black ash from other ash and hardwood species using G-LiHT data. Despite smaller than desired sample sizes we were able to achieve comparable accuracies to similar studies in a novel environment and show that object-based classification methods using hyperspectral data are a viable method for mapping ash species distribution moving forward. With additional samples and the possible inclusion of time series imagery or site variables, accuracies can be increased even further to provide for precision mapping of individual black ash trees.

CHAPTER 3 MAPPING ASH SPECIES ACROSS A MIXED FOREST USING MULTISPECTRAL IMAGERY

3.1. Introduction

As described in Chapter 2, because of dispersed growing pattern of ash and the predominance of other tree species, high spatial resolution remote sensing data are needed to identify ash trees at the genus level (Lisein et al. 2015; Murfitt et al. 2016; Sapkota and Liang 2020). Remotely sensed multispectral imagery has a strong history of being used to classify individual tree species in various settings (Franklin et al. 2000; Immitzer et al. 2012; Yang et al. 2014a). Multispectral data are typically less costly and easier to acquire compared to hyperspectral data and their processing is less computationally expensive and therefore if ash trees can be identified using these types of data, classification can be made easier and economically more affordable. Multispectral data have been used to identify individual ash trees in Arkansas, United States (Sapkota and Liang 2020) and in Europe (Waser et al. 2014), in addition to assessing ash tree health (Murfitt et al. 2016; Pontius 2014).

WV-2 provides multispectral images in eight spectral bands (red (659 nm), green (546 nm), blue (478 nm), coastal blue (427 nm), yellow (608 nm), red-edge (724 nm), near-infrared 1 (831 nm), and near-infrared 2 (908 nm)) at roughly 1.84 m resolution and a panchromatic band at roughly 0.46 m resolution (DigitalGlobe 2009). While WV-3 has slightly higher spatial resolution than WV-2 (0.31m in the panchromatic band compared to 0.46m respectively), the resolutions are significantly smaller than the average tree crown widths in Maine (Russell and Weiskittel 2011) and so should be sufficient to generate helpful structural data (Li et al. 2015).

While this is not the first attempt to use multispectral imagery to identify ash at the individual tree level (Sapkota and Liang 2020), nor to specifically identify black ash (Engelstad et al. 2019; Host et al. 2020), to our knowledge this is the first attempt to use multispectral

imagery to identify and classify black ash at the individual tree level. Sapkota and Liang (2020) used similar data (WV-3) and identified individual ash trees, but did not attempt to differentiate the individual ash species from one another. Likewise, both Engelstad et al. (2019) and Host et al. (2020) did identify black ash, but did so using 30 m resolution Landsat data in a relatively homogenous environment. Similar studies seeking to identify black ash habitat in Maine have utilized geographical information system (GIS) based techniques, such as incorporating depth to water table or similar metrics (Costanza 2015). As such, we believe that this is the first study to identify ash species and black ash in particular using WV-2 imagery. The specific objectives are: 1) create and evaluate both pixel-based and object-based classification models for tree species identification with the focus on ash trees and 2) evaluate different non-parametric algorithms for tree identification.

3.2. Materials and methods

3.2.1. Field work

The study sites and field dataset are the same as described in Chapter 2 Section 2.2.1. Due to the presence of clouds in the northern parts of the imagery taken over Site 1, numerous GPS tagged trees in that Site had to be discarded, resulting in a smaller number of samples utilized (Table 3.1). Classes and class totals reflect those trees that could be successfully identified and delineated, grouped together with respect to sample size and spectral similarity for classification purposes.

Table 3.1 Field data tree species collected for training and model validation (left) and aggregated classes and number of samples used for classification (right) for WV-2 data

Species	Species Class	Species Totals	Class	Sample Totals
Quaking aspen	Quaking aspen	22	Ash (AS)	35
Balsam fir	Softwood	35	Quaking aspen (QA)	22
Black ash	Ash	63	Other Hardwood (HW)	21
Green ash	Ash	25	Red maple (RM)	33
Eastern hemlock	Softwood	25	Softwood (SW)	41
Northern white cedar	Softwood	44		
Oak spp.	Other Hardwood	4		
Paper birch	Other Hardwood	7		
Red maple	Red maple	50		
Red spruce	Softwood	8		
White ash	Ash	21		
White pine	Softwood	6		
Yellow birch	Other Hardwood	15		
Total		316		

3.2.2. Remote sensing data and data pre-processing

In this study we utilized multispectral data from the WV-2 satellite imaging system, collected June 25, 2015. The workflow for this Chapter is diagrammed for improved understanding (Figure 3.1). The data were received from DigitalGlobe atmospherically corrected and orthorectified, so no further correction was needed. The image was provided in multispectral and panchromatic rasters.

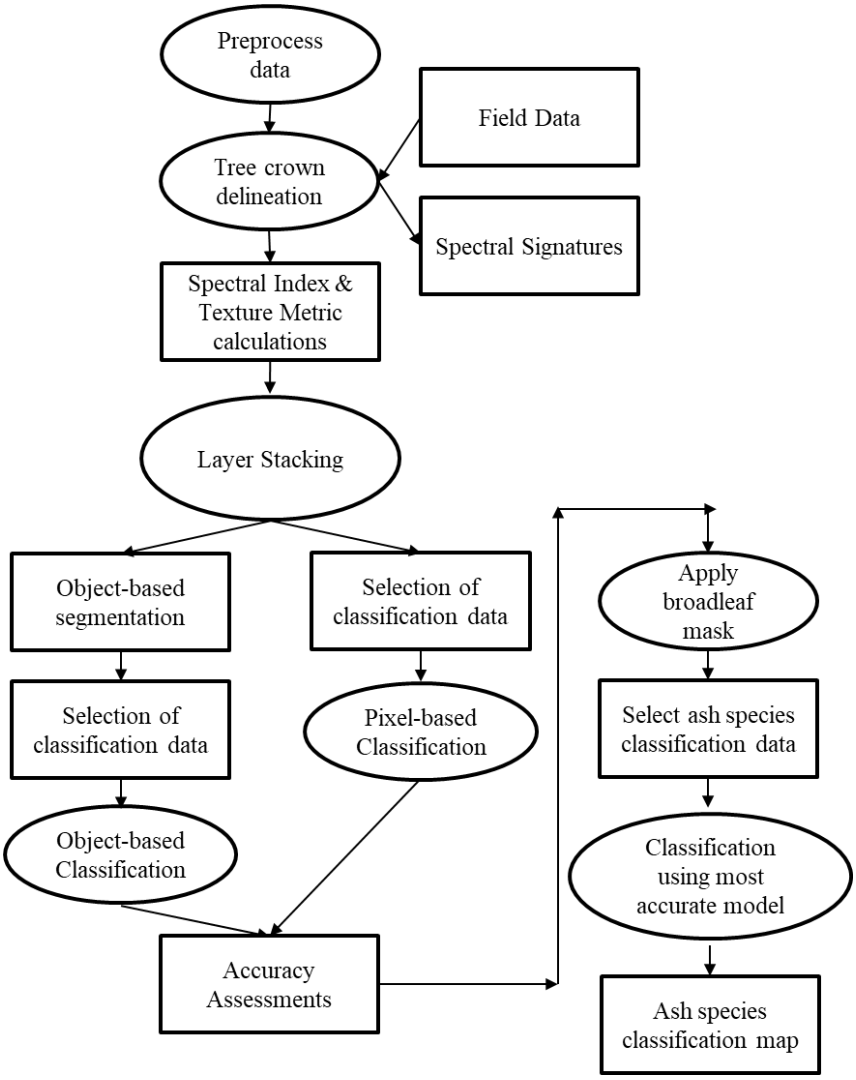

Figure 3.1 Workflow for development of ash tree species maps using WV-2 multispectral data

The rest of the pre-processing was completed using ENVI version 5.5.2. First, the individual study sites were clipped from the larger rasters, and the Gram-Schmidt pan sharpening technique was used to fuse the multispectral and panchromatic images together, resulting in a ~0.6 m spatial resolution multispectral image that retains the spectral information present in the original image while matching the spatial resolution to the panchromatic band (Aiazzi et al. 2009). Then a suite of SVIs and texture metrics were calculated (Table 3.2 and Table 3.3). The SVIs, texture metrics, and spectral bands were stacked, creating a 58 layer data cube. The choice of the indices and texture metrics was based on their performance in previous research. Sapkota

and Liang (2020) showed that the inclusion of texture metrics such as those described in Table 3.3 significantly increased the accuracy of ash classification.

Table 3.2 Spectral vegetation indices calculated using WV-2 imagery

Name	Equation	Reference
NDVI[S]	$\frac{NIR_1 - R}{NIR_1 + R}$	Rouse et al. (1974)
GNDVI[S]	$\frac{NIR_1 - G}{NIR_1 + G}$	Gitelson and Merzlyak (1994)
EVI[S]	$2.5 * \left(\frac{NIR_1 - R}{NIR_1 + R * 6.0 - 7.5 * B}\right)$	Huete et al. (1994)
IPVI[P]	$\frac{NIR_1}{NIR_1 + R}$	Crippen (1990)
GRR[S]	$\frac{G}{R}$	Waser et al. (2014)
RR[S]	$\left(\frac{NIR_1}{R}\right) * \left(\frac{G}{R}\right) * \left(\frac{NIR_1}{RE}\right)$	Waser et al. (2014)
PSRI[P]	$\frac{R - B}{RE}$	Merzlyak et al. (1999)
RENDVI[S]	$\frac{NIR_1 - RE}{NIR_1 + RE}$	Gitelson and Merzlyak (1994)
RVI[S]	$\frac{NIR_1}{R}$	Jordan (1969)
REVI[S]	$\frac{NIR_1 - R}{\sqrt{(NIR_1 + R)}}$	Roujean and Breon (1995)
ARVI[P]	$\frac{NIR_1 - \left(R(B - R)\right)}{NIR_1 + \left(R - (B - R)\right)}$	Kaufman and Tanre (1992)
REYR[S]	$\frac{RE - Y}{RE + Y}$	Gwata (2012)
DDVI[P]	$(2 * NIR_1 - R) - (G - B)$	Le Maire et al. (2004)
WIVI[S]	$\frac{NIR_2 - Red}{NIR_1 + Red}$	Wolf (2012)

NDVI = Normalized Difference Vegetation Index, GNDVI = Green Normalized Difference Vegetation Index, EVI = Enhanced Vegetation Index, IPVI = Infrared Percentage Vegetation Index, GRR = Green-Red ratio, Red ratio = Red Ratio, PSRI = Plant Senescence Reflectance Index, RENDVI = Red-Edge Normalized Difference Vegetation Index, RVI = Ratio Vegetation Index, REVI = Renormalized Vegetation Index, ARVI = Atmospherically Resistant Vegetation Index, REYR = Red-Edge-Yellow ratio, DDVI = Difference Difference Vegetation Index, WIVI = Worldview Improved Vegetative Index.

[P] The index measures physiological traits such as pigment or chlorophyll concentrations.

[S] The index measures physical traits such as leaf area index (LAI).

Table 3.3 Texture metrics for classification using WV-2 imagery

Texture Metric	Equation	Reference
1st Order Data Range (Red, Red Edge, NIR_1)	$Max - min$	Anys et al. (1994)
1st Order Mean (Red, Red Edge, NIR_1)	$\sum_{i=0}^{N_g-1} iP(i)$	Anys et al. (1994)
1st Order Variance (Red, Red Edge, NIR_1)	$\sum_{i=0}^{N_g-1} (i-M)^2 P(i)$	Anys et al. (1994)
1st Order Entropy (Red, Red Edge, NIR_1)		Anys et al. (1994)
2nd Order Mean (Red, Red Edge, NIR_1)	$\sum_{i=1}^{N_g}\sum_{j=1}^{N_g} i * P(i,j)$	Haralick et al. (1973)
2nd Order Variance (Red, Red Edge, NIR_1)	$\sum_{i=1}^{N_g}\sum_{j=1}^{N_g} (i-\mu)^2 P(i,j)$	Haralick et al. (1973)
2nd Order Homogeneity (Red, Red Edge, NIR_1)	$\sum_{i=1}^{N_g}\sum_{j=1}^{N_g} \frac{1}{1+(i-j)^2} P(i,j)$	Haralick et al. (1973)
2nd Order Contrast (Red, Red Edge, NIR_1)	$\sum_{i=1}^{N_g}\sum_{j=1}^{N_g} P(i,j)(i-j)^2$	Haralick et al. (1973)
2nd Order Dissimilarity (Red, Red Edge, NIR_1)	$\sum_{i=1}^{N_g}\sum_{j=1}^{N_g} P(i,j)\lvert i-j\rvert$	Haralick et al. (1973)
2nd Order Entropy (Red, Red Edge, NIR_1)	$\sum_{i=1}^{N_g}\sum_{j=1}^{N_g} P(i,j)\log(P(i,j))$	Haralick et al. (1973)
2nd Order Second Moment (Red, Red Edge, NIR_1)	$\sum_{i=1}^{N_g}\sum_{j=1}^{N_g} \{P(i,j)\}^2$	Haralick et al. (1973)
2nd Order Correlation (Red, Red Edge, NIR_1)	$\frac{\sum_{i=1}^{N_g}\sum_{j=1}^{N_g}(ij)P(i,j) - \mu_x\mu_y}{\sigma_x\sigma_y}$	Haralick et al. (1973)

Where P(i) = probability of each pixel value; N_g = number of distinct grey levels in the quantized image; i and j = the row and column numbers in the spatial matrix; p(i,j) = the value of cell i,j in the matrix; μ = the mean; and σ = the standard deviation.

3.2.3. Pixel-based classification methods

Individual tree crowns were identified with the help of the GPS points collected in the field using ENVI 5.5.2. Due to the condensed and overlapping nature of many of the tree canopies in the study area, only trees in the Dominant or Co-Dominant crown classes were considered and extreme care was taken to ensure accurate attribution. Trees were classed into groups (Table 3.1), with the ash species grouped together only for the initial classification. Individual tree crowns were identified and delineated using the true-color red-green-blue image. These crowns were used to create mean spectral signatures for each target class and to extract pixel data from the multispectral data stack for classification purposes.

3.2.4. Object-based classification methods

For a detailed explanation of L3Harris GeoSpatial's ENVI 5.5 Feature Extraction module, please refer to Chapter 2 Section 2.2.4. For this analysis, the entire 58-layer multispectral, spectral index, and texture metric stack was used as input for segmentation. Segmentation was again performed at scale 10 with no merge. Training data were extracted using the delineated tree crowns previously identified.

3.2.5. Classification modeling

Once all input variables were prepared for pixel-based and object-based approaches, we implemented classification (Blaschke and Hay 2001) using RF and SVM as described in Chapter 2 Section X.X. Each classification data set was randomly split into 60% training data and 40% testing data and each model was trained using 10-fold repeated cross validation.

A set of statistical measures were calculated for each algorithm, namely mean kappa, mean accuracy, out-of-bag error (for RF), and confusion matrices. Based on these statistics the most accurate classification method was selected and utilized in black ash identification.

3.2.6. Black ash classification

In order to differentiate black ash, we first created a mask of only those pixels representing broadleaf tree crowns, as determined by the initial round of classification using the most accurate model. After determining that object-based methods created the most realistic ash genus classification map, training data for each ash species were selected. Due to spectral similarity and class size concerns, we combined green and white ash, red maple, and the other hardwood classes into a single class, with 30% of each species being randomly selected to achieve a balanced class, both in terms of internal species composition and compared to the other (BA and QA) classes (Table 3.4). In addition, 50% (rather than 40%) of the data were reserved for validation purposes due to concerns about having adequate validation data. Classification proceeded in an otherwise identical fashion to the first round with broadleaf and ash species.

Table 3.4 Classification species groups for black ash species identification, and total number of samples

Class	Sample Totals
Black ash (BA)	15
Quaking aspen (QA)	22
Red maple, green and white ash, and other hardwood (HW)	24

3.3. Results

3.3.1. Evaluation of WV-2 spectral bands for ash genus classification

Spectral signatures for all classes were calculated (Figure 3.2) using eight pan-sharpened WV-2 spectral bands and the same training data used for pixel-based classification. As expected, most of the genera (AS, HW, RM, and QA) are largely aligned throughout the optical spectrum but differentiation is observed from 500-600nm and 730 – 900nm, especially between the SW and other classes.

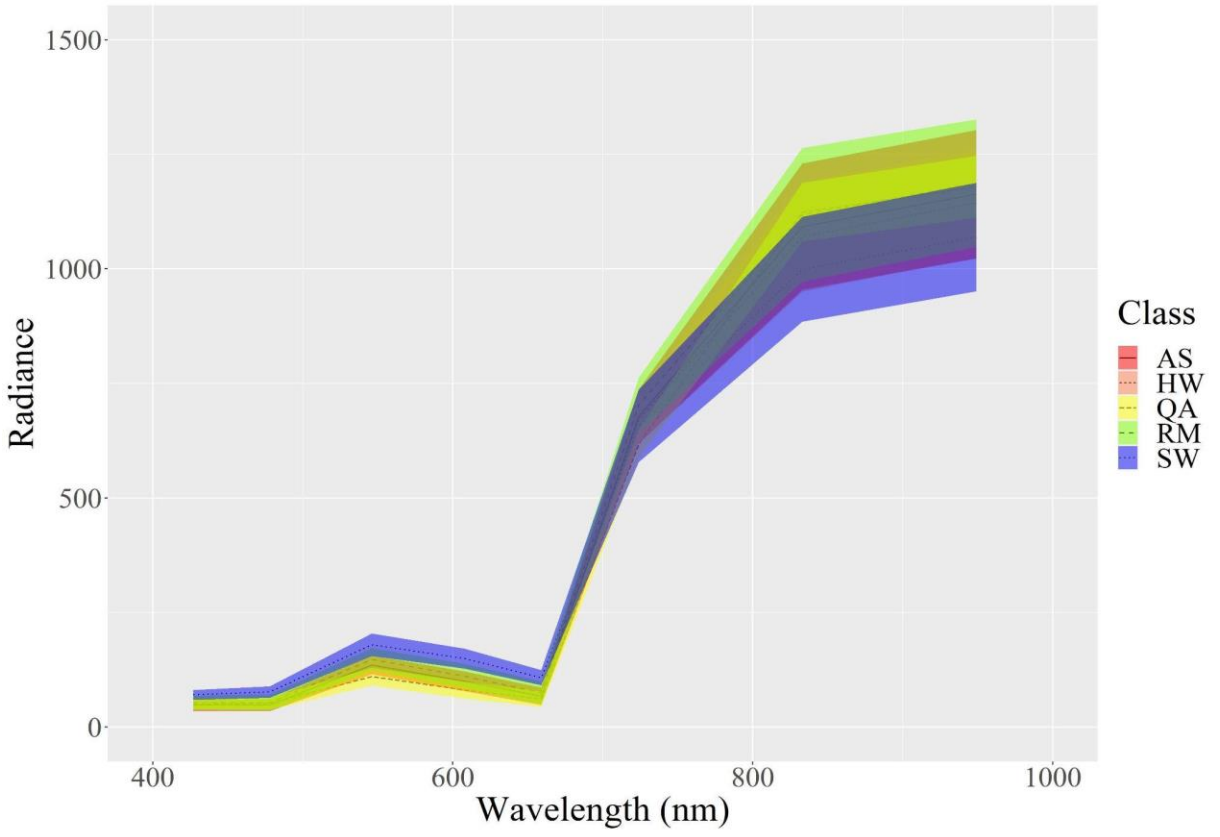

Figure 3.2 Mean spectral signatures of ash and co-occurring genera, derived from WV-2 multispectral data. Shaded area equates to Mean +/- Standard Deviation.

Statistical analysis was performed on each class pair, and significant differences in band pairings were calculated (Figure 3.3). Hardwood (AS, RM, HW) classes show significant differences with both QA and SW, and SW and QA are significantly different from each other (Figure 3.3).

Among the hardwood classes (AS, RM, HW), AS and RM are significantly different from each other, as are HW and RM, in a number of bands. This suggests that spectral information will be key in separating out at least a number of classes. However, no significantly different bands were identified between the AS and HW classes over the spectrum.

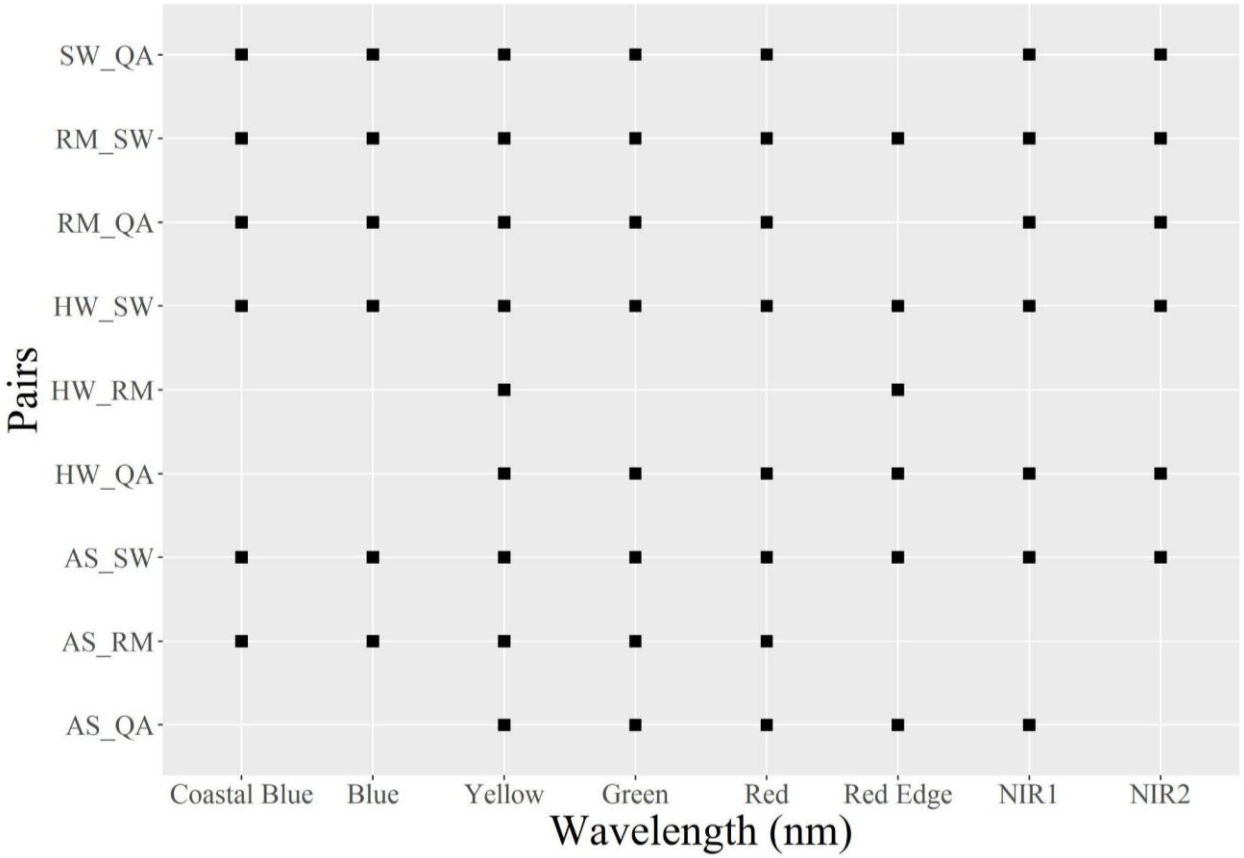

Figure 3.3 Significance of spectral signature difference between ash and co-occurring genera. Points indicate statistically significant differences between class pairs (P<0.05). No statistically different band pairs were found for AS_HW.
NIR1 = Near Infrared 1, NIR2 = Near Infrared 2.
AS = ash, HW = hardwood, QA = quaking aspen, RM = red maple, SW = softwood

The top 25 variables as determined by their importance to the RF classification were graphed according to their mean accuracy (Figure 3.4). Multiple texture metrics, spectral indices, and spectral bands are present, suggesting each set of data is critical in achieving model success.

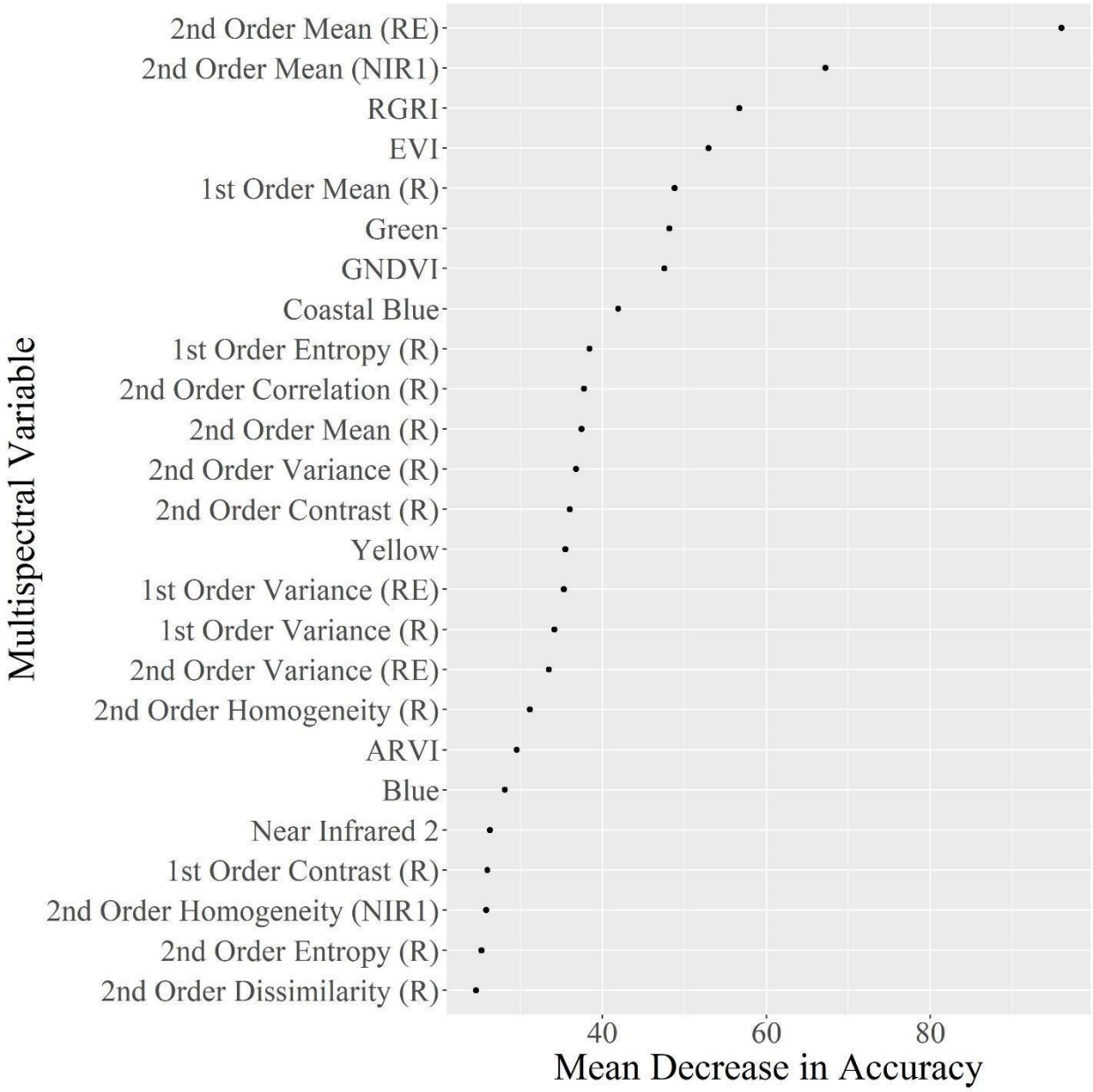

Figure 3.4 Top 25 multispectral variables, derived from RF pixel-based classification. Top 25 variables shown for visual purposes – models using only the top 25 variables did not result in statistically different classification accuracies.

3.3.2. Segmentation results

Multiple segmentation scales were utilized to determine the best scale for individual tree delineation. Scale 5 (Figure 3.5a) shows over-segmentation even on small crowns and scale 20 (Figure 3.5c) shows significant (and unacceptable) under-segmentation. While scale 10 (Figure 3.5b) did over-segment large crowns, this was expected (Yang et al. 2015) and scale 10 showed the greatest ability to identify individual crowns while not producing an overwhelming amount of over-segmentation.

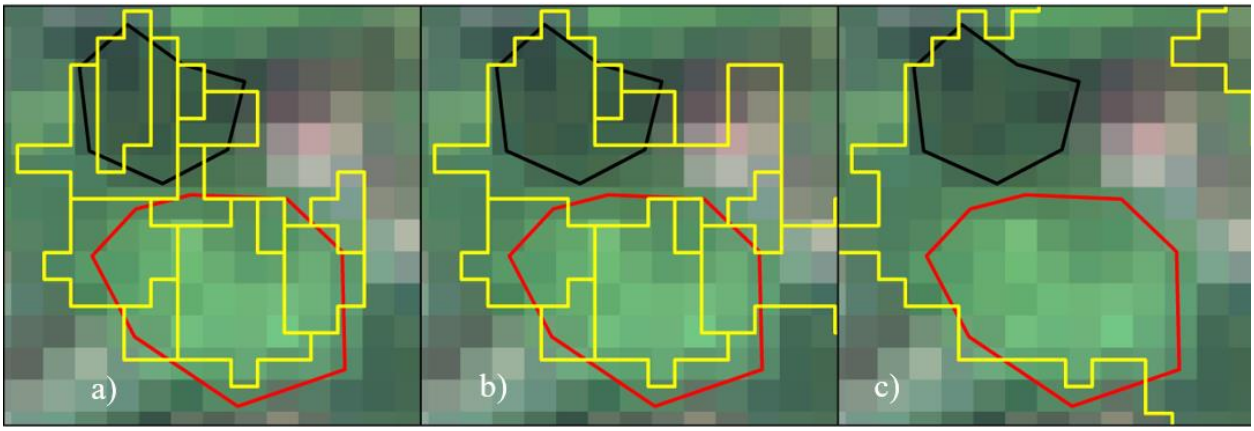

Figure 3.5 Comparison of segmentation scale factors, red = ash tree crown, black = gap in canopy.

3.3.3. Ash species classification

After all areas identified as SW were removed from the image, the tree crown polygons were used to extract spectral signatures for each broadleaf species using the pan-sharpened WV-2 multispectral data (Figure 3.6). Green and white ash were separated into a distinct class (AS) from black ash (BA), and the SW class was excluded from this portion of the analysis.

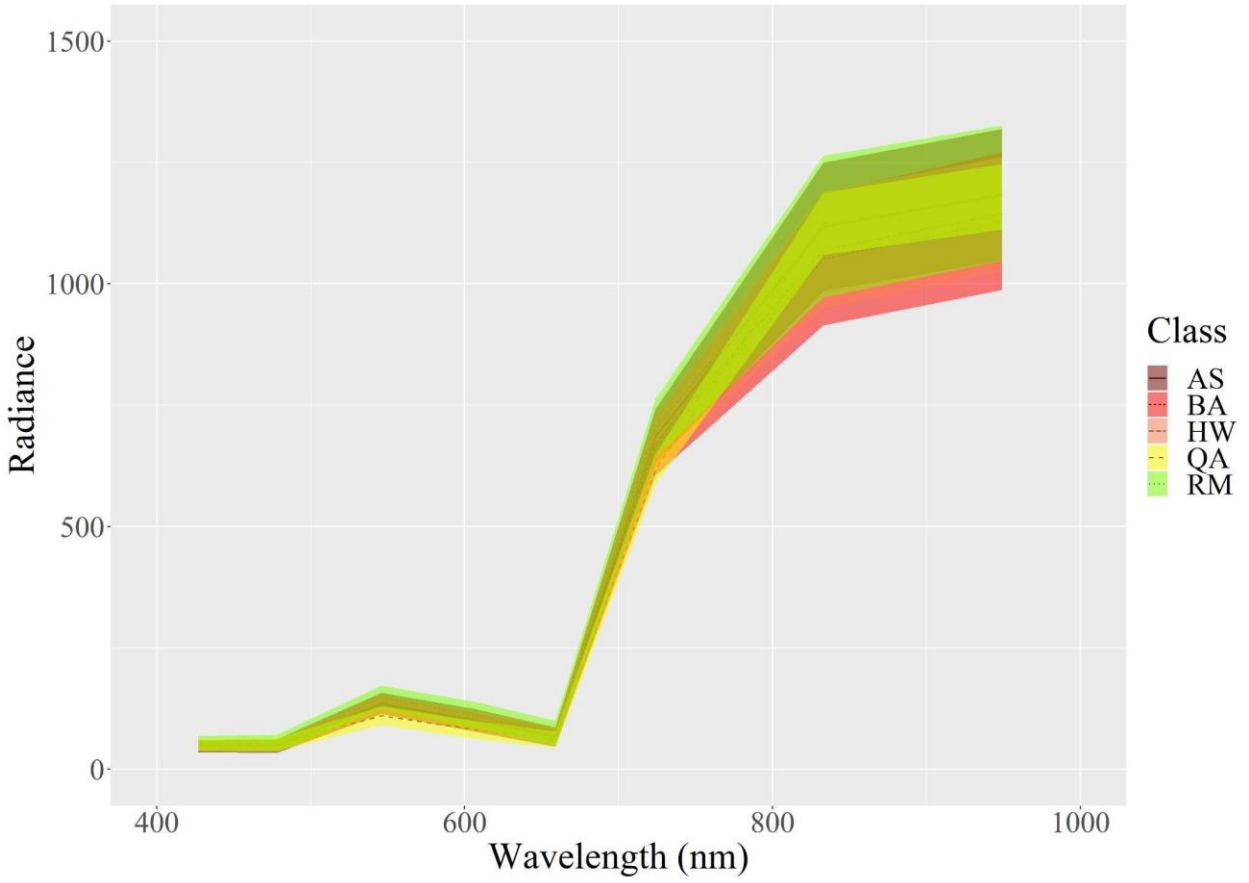

Figure 3.6 Mean spectral signatures of different ash species and other co-occurring species derived from WV-2 multispectral data. Shaded area equates to Mean +/- Standard Deviation. AS = green and white ash, BA = black ash, HW = other hardwood, RM = red maple, and QA = quaking aspen.

Statistical analysis of the band pairs was performed and the results were graphed (Figure 3.7). BA shows significant separation from RM and QA, and all classes show significant differences from QA in at least one band (Figure 3.7). However, the AS, RM, and HW classes were found to be similar over the entire spectrum.

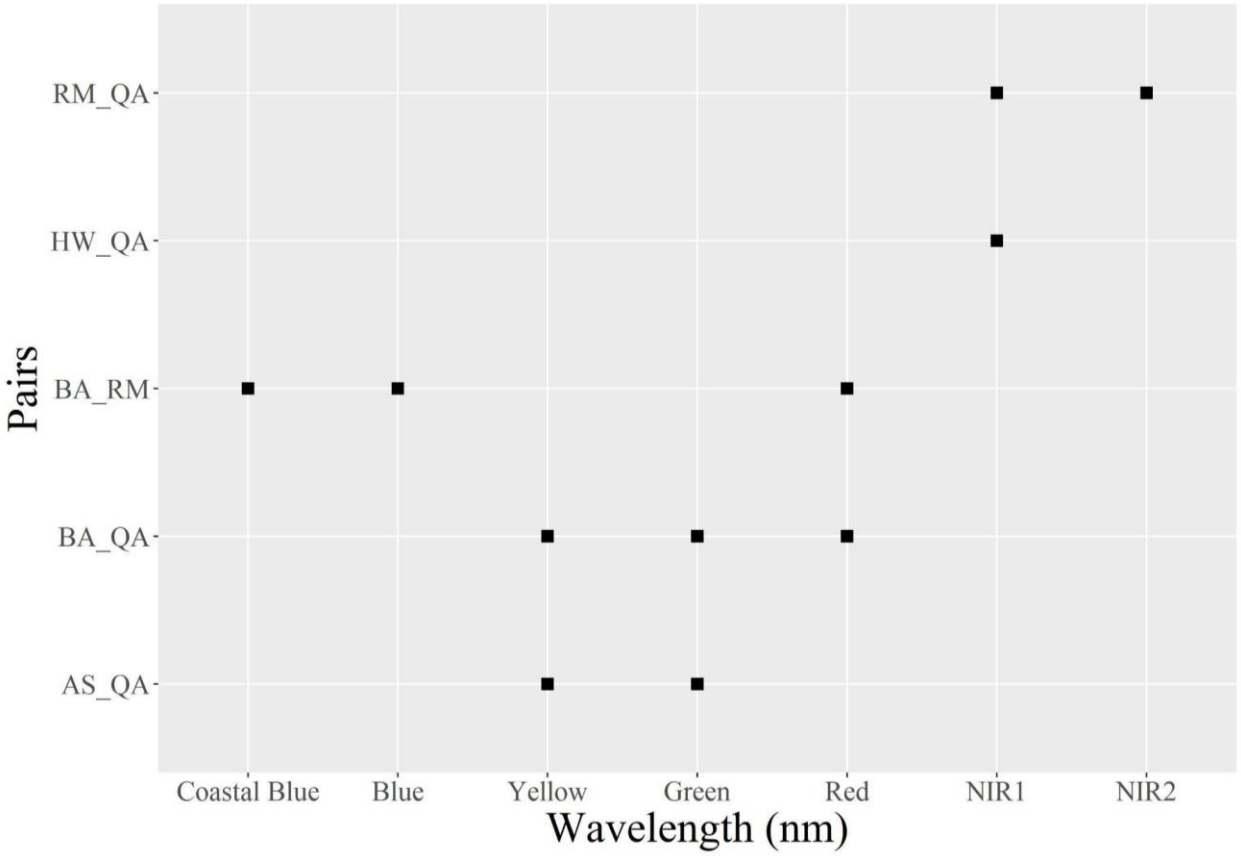

Figure 3.7 Significance of spectral signature difference between black ash, other ash species, and other co-occurring species. Points indicate statistically significant differences between class pairs (P<0.05). No statistically different wavelength pairs were found for AS_HW, AS_RM, BA_AS, BA_HW, and HW_RM. AS = green and white ash, BA = black ash, RM = red maple, QA = quaking aspen, and HW = other hardwood.

3.3.4. Genera classification

Externally derived accuracy metrics and confusion matrices of the pixel-based classification methods were calculated (Table 3.5), along with internally derived mean accuracies and kappa values (Table 3.6). The RF pixel-based model produced an overall accuracy and kappa coefficient of 63% and 0.53, respectively. The AS, HW, and RM classes experienced some confusion, with AS and RM confusion being the most common error.

The SVM pixel-based model produced similar results, achieving an overall accuracy of 62.4% and a kappa value of 0.52. SVM experienced significant difficulties classifying the HW class and both methods had trouble separating RM from AS.

The externally derived confusion matrices and accuracy metrics of the object-based classification methods were also calculated (Table 3.7), along with the internally-derived mean accuracies and kappa values (Table 3.8). Again the models performed similarly, with RF achieving an accuracy and kappa of 61.2% and 0.50, respectively and SVM achieving 61.9% and 0.52, respectively. Object-based methods still confused the AS, RM, and HW classes, but to a lesser extent than pixel-based methods.

To demonstrate the distribution of internally-derived accuracies each value was graphed, with letters indicating groups of statistically similar classifiers (Figure 3.8). All models produced closely aligned results, as evidenced by the statistical similarity. Classification maps of the most accurate pixel- and object-based classification methods (SVM), with subsets comparing RF- and SVM- derived maps, were produced (Figure 3.9 and 3.10). Despite the lack of clear statistical evidence, SVM was deemed the most accurate model due to both the RF models producing large areas of homogenous species that were inconsistent with any areas encountered during the course of fieldwork. In addition, the pixel-based SVM model produced large areas of ash that were

similarly not encountered in the field. The object-based SVM model, however, produces a classification more closely aligned to researcher's understanding and experience of the site.

Table 3.5 Confusion matrices and accuracy metrics of WV-2 pixel-based classification methods for ash genus classification based on external validation. PA = Producer's Accuracy, UA = User's Accuracy

Model	Species	AS	HW	QA	RM	SW	UA (%)
Pixel + RF	AS	6	3	0	5	0	42.9
	HW	3	3	0	3	1	30.0
	QA	0	0	8	0	0	100
	RM	5	0	0	4	0	44.4
	SW	1	3	1	2	17	70.8
	Total	15	9	9	14	18	
	PA (%)	40.0	33.3	88.9	28.6	94.4	
Overall accuracy **58.5%**, and kappa coefficient 0.47							
Pixel + SVM	AS	6	5	0	7	0	33.3
	HW	0	0	0	0	0	0
	QA	0	0	7	0	0	100
	RM	8	2	0	5	0	33.3
	SW	1	2	2	2	18	72
	Total	15	9	9	14	18	
	PA (%)	40.0	0.0	77.8	35.7	100	
Overall accuracy **55.4%** and kappa coefficient 0.42							

Table 3.6 Internally-derived accuracy metrics (Mean ± Standard Deviation) for WV-2 pixel-based ash species classification methods

Model	Accuracy (%)	kappa	Out-of-bag error (%)
Pixel + RF	63.0 ± 13.4	0.53 ± 0.17	36.7
Pixel + SVM	62.4 ± 12.7	0.52 ± 0.16	

.

Table 3.7 Confusion matrices and accuracy metrics of WV-2 object-based classification for ash genus classification methods. PA = Producer's Accuracy, UA = User's Accuracy

Model	Species	AS	HW	QA	RM	SW	UA (%)
Object + RF	AS	8	2	0	4	1	53.3
	HW	1	4	0	0	0	80.0
	QA	0	1	8	0	1	80.0
	RM	4	0	0	6	0	60.0
	SW	1	1	0	3	14	73.7
	Total	14	8	8	13	16	
	PA (%)	50.0	50.0	100	46.2	87.5	
Overall accuracy **67.8%** and kappa coefficient 0.59							
Object + SVM	AS	7	2	0	3	1	53.8
	HW	3	4	0	4	1	33.3
	QA	0	1	8	0	1	80.0
	RM	4	1	0	3	3	27.3
	SW	0	0	0	3	10	76.9
	Total	14	8	8	13	16	
	PA (%)	50.0	50.0	100	23.1	62.5	
Overall accuracy **54.2%** and kappa coefficient 0.43							

Table 3.8 Internally-derived accuracy metrics (Mean ± Standard Deviation) for WV-2 pixel-based ash species classification methods

Model	Accuracy (%)	kappa	Out-of-bag error (%)
Object + RF	61.2 ± 13.7	0.50 ± 0.18	37.6%
Object + SVM	61.9 ± 12.6	0.52 ± 0.16	

Pixel-based approaches slightly outperformed object-based approaches in terms of overall accuracy, however not to a statistically significant extent (Figure 3.10). The QA and SW classes were clearly differentiated from the other hardwood classes (AS, RM, HW) and each other by all methods, while the other hardwood classes experienced class mixing. While the object-based RF method did produce the highest external accuracy, the resultant classification map showed far less class sensitivity compared to the object-based SVM method. As such, object-based SVM was chosen to move forward with black ash classification (and the pixel-

based SVM model is shown for comparison). Despite the range in external validation statistics between models (Table 3.6 and 3.8), none of the models produce statistically different internal accuracy metrics (Figure 3.8).

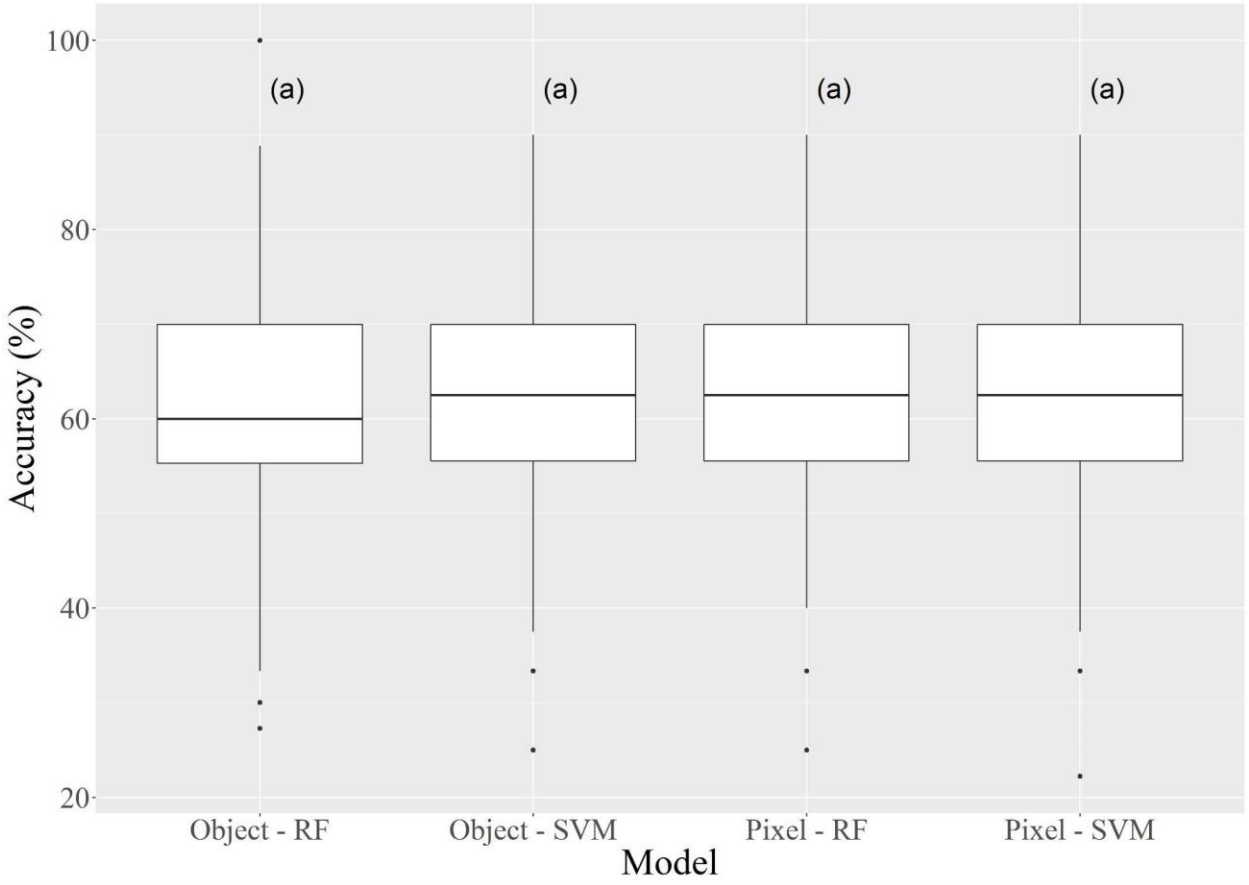

Figure 3.8 Distribution of WV-2 based model accuracies derived from internal 10-fold validation. Letters indicate statistically similar models.

Ash and co-occurring genera were successfully classified using multiple methodologies (Figures 3.9 and 3.10). While there is some visible class switching between the hardwood classes (RM, AS, and HW), the classifications are generally stable. Confidence in the models are supported by the species differentiation between sites, as Site 1 has significantly more QA compared to Site 2 and Site 2 is dominated by SW and AS.

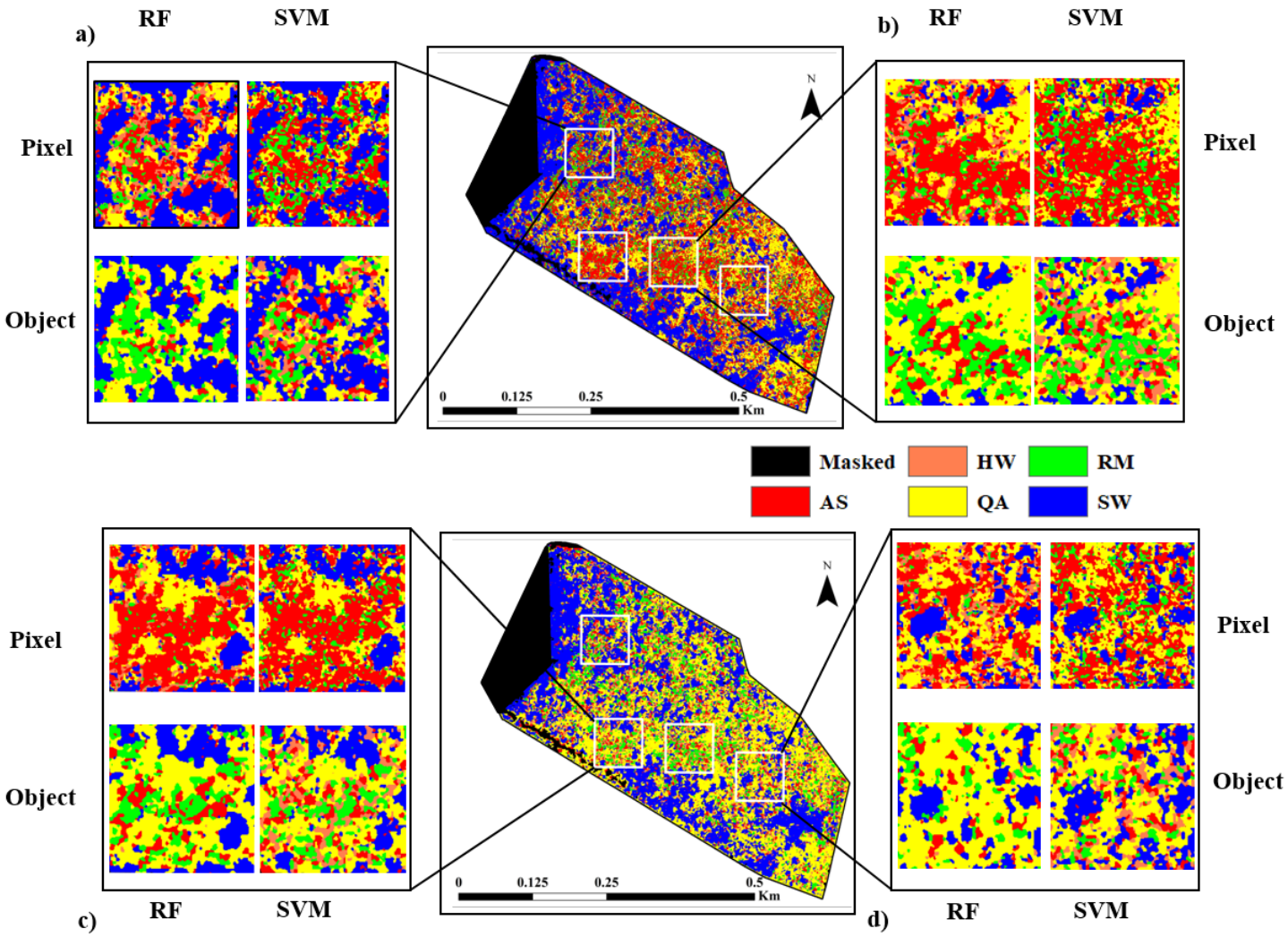

Figure 3.9 Classification map of Site 1 using WV-2 multispectral data and varied classification methods. Top center = pixel-based SVM, bottom center = object-based SVM. Focus areas were chosen to highlight different aspects of model:
a) Consistency in softwood but inconsistency in hardwood classes; b) Small riparian area, consistent hardwood classification but confusion between classes; c) Aspen and softwood classes are highly consistent; and d) Object-based approaches losing variation in species patterns being detected by pixel-based classifiers.

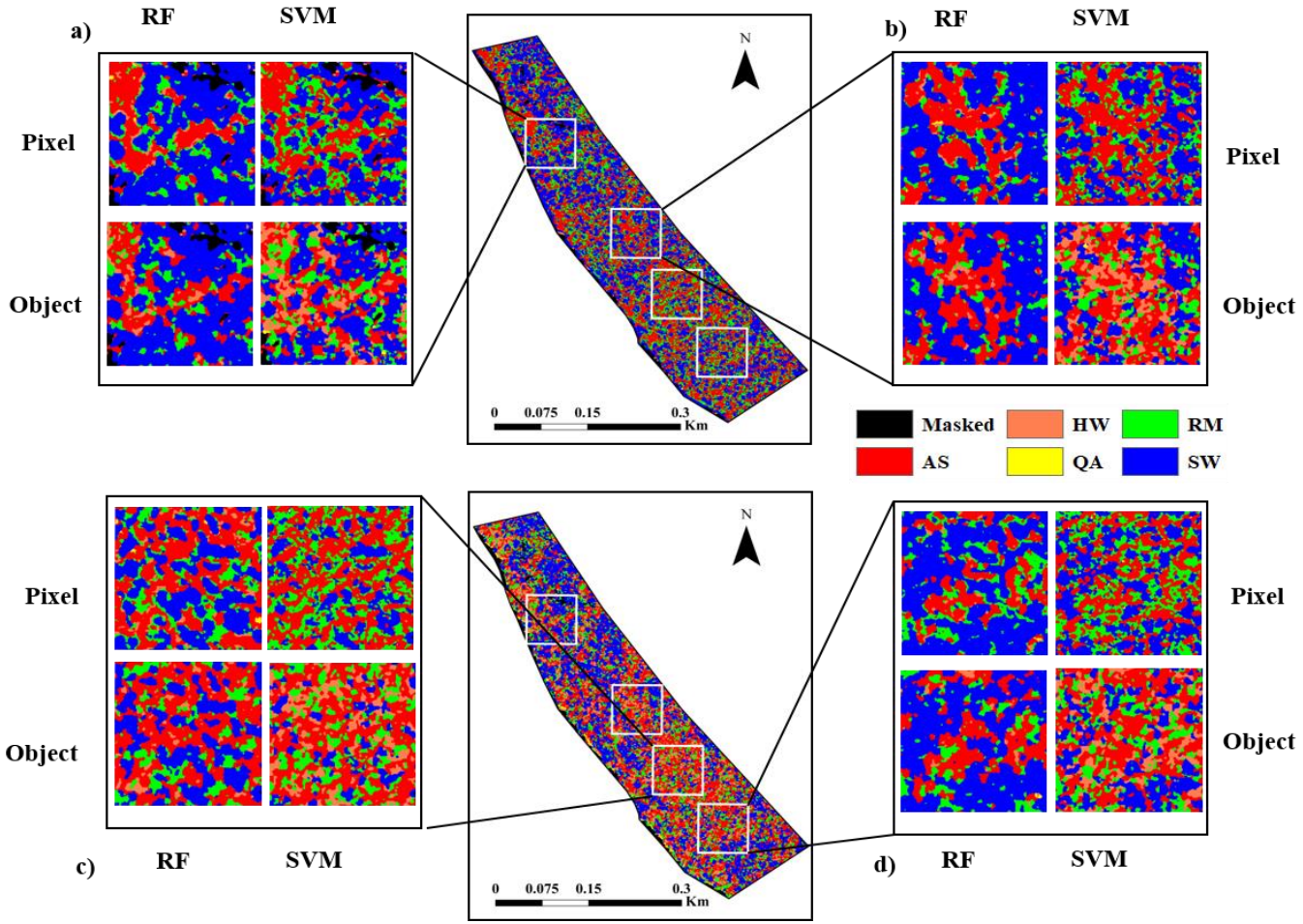

Figure 3.10 Classification map of Site 2 using WV-2 multispectral data and varied classification methods. Top center = pixel-based SVM, bottom center = object-based SVM. Focus areas were chosen to highlight different aspects of model (clockwise from top left): a) Overall consistency of classification, with pixel-based and SVM approaches detecting additional variation; b) Confusion between ash, maple, and hardwood classes; c) Some class switching between hardwoods, RF-pixel based detecting some aspen; and d) Confusion between ash, maple, and hardwood classes.

3.3.5. Black ash classification

Utilizing an object-based SVM classifier, BA was classified with 57.1% Producer's Accuracy and an overall accuracy of 75.9% (Table 3.9). There is still some confusion between the BA and HW class, as was seen in the initial round of classification and likely exacerbated by the inclusion of green and white ash into the HW class. Classification maps show the dominance of BA in Site 2, compared to the relative dominance of QA and HW in Site 1 which lends additional credence to the model (Figure 3.11). Site 2 contained relatively more black ash (as compared to white and green) and virtually no quaking aspen and Site 1 contained large amounts of quaking aspen and a higher proportion of green and white ash compared to Site 2.

Table 3.9 Confusion matrix and accuracy metrics of black ash classification based on WV-2 data

Model	Species	BA	HW	QA	UA (%)
Object + SVM	BA	4	4	0	50.0
	HW	3	7	0	70.0
	QA	0	0	11	100.0
	Total	7	11	11	
	PA (%)	57.1	63.6	100.0	
Overall accuracy **75.9%** and kappa coefficient **0.64**					

Table 3.10 Internally-derived accuracy metrics (Mean ± Standard Deviation) for black ash identification using WV-2 data

Model	Accuracy (%)	kappa
Object + SVM	66.0 ± 26.7	0.47 ± 0.40

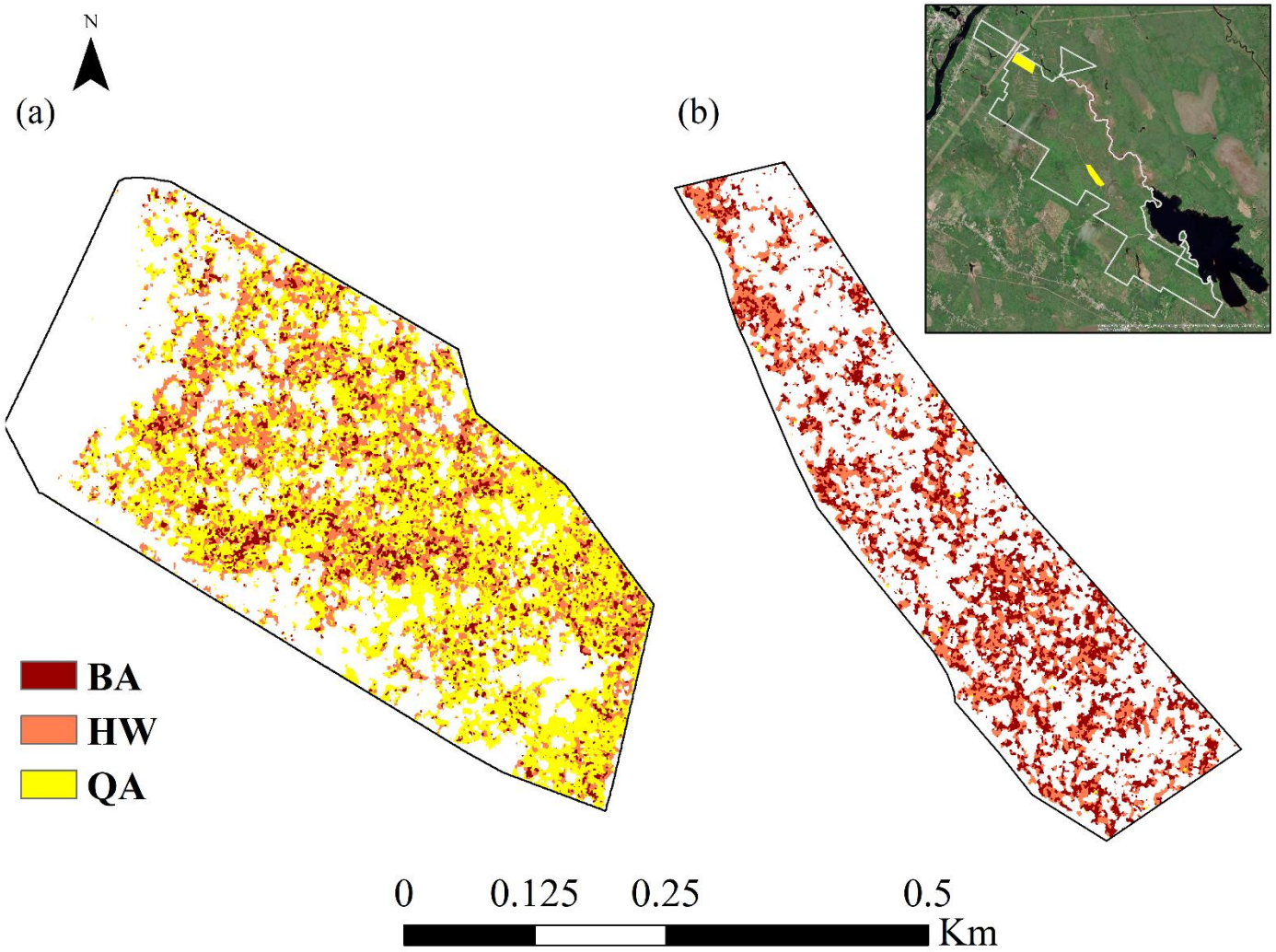

Figure 3.11 Black ash classification maps utilizing WV-2 object-based, SVM algorithm of a) Site 1 and b) Site 2

3.4. Discussion

3.4.1. Object- vs. pixel-based classification

In achieving overall accuracies of approximately 61 and 62% (Table 3.8) utilizing object- and pixel-based classification approaches, we have shown that classifying individual trees at a species level is possible with WV-2 data. When using object-based methods we achieved similar overall accuracy results compared to other studies utilizing WV-2 (63%, Murfitt et al. (2016)) and lower accuracy results than studies using WV-3 (82%, Sapkota and Liang (2020)) data. Pixel-based classification approaches, although slightly higher in mean accuracy, did not perform significantly better. It is possible this improvement in accuracy is due to the segmentation step in object-based methods having difficulty in segmenting and merging very large and very small objects within the same scene. Both study sites had a large range in crown sizes of target trees – from black ash with only a few square meters of canopy to large white pines or hemlock with 10 m canopy radii – and, critically, many overlapping canopies. It is possible that pixel-based methods were able to slightly better handle the complexity of the mixed forest than object-based methods.

However, both of the aforementioned studies - Murfitt et al. (2016) and Sapkota and Liang (2020) - had larger sample sizes than the current study which likely played a role in the higher accuracy values achieved by those researchers. Murfitt et al. (2016) used 131 ash trees while Sapkota and Liang (2020) used 230, compared to 35 ash trees in this study (some of the initially collected data was not used due to the inability to positively delineate and attribute specific tree crowns to GPS points, and other data had to be discarded due to cloud cover in the WV-2 imagery). It is worth noting that when Sapkota and Liang (2020) limited their sample size

to 50 ash trees they achieved 50% overall accuracy, whereas this study achieves roughly 61% overall accuracy with a similar, but smaller, sample size.

3.4.2. RF vs. SVM classification

Neither RF nor SVM methods produced statistically different results, yet the maps produced show clear differences in classification. SVM classification produces far more variation in classes compared to RF both in pixel- and object- based methods. RF is a versatile, decision tree based model that is able to handle lots of data in a variety of settings and formats (Breiman 2001), but may not be able to capture subtle class variation in the same way that SVM does. SVM is more computationally intensive but can achieve higher accuracy at lower sample sizes and handle unbalanced classes better compared to RF (Nitze et al. 2012; Thanh Noi and Kappas 2018).

3.4.3. Ash genus identification

This study shows that WV-2 multispectral data can be used to classify ash and co-occurring tree genera. We observed some class disagreement in some of the hardwood (ash, maple, mixed hardwood) classes. As the mixed hardwood class is dominated by paper and yellow birch, seeing these classes mix is expected due to spectral similarities between the *Fraxinus* and *Betula* genera (Maschler et al. 2018), but still undesirable. The model stability in terms of hardwood/softwood classification is strong, however, suggesting that, at minimum, the model could be used to accurately map areas where there is a high likelihood of ash being present.

3.4.4. Black ash identification

This study suggests that multispectral imagery can be used to map ash species composition with moderate success. Accuracy metrics show that black ash is being separated from other hardwoods with some success despite confusion between the HW and BA classes. That being said, the resultant classification map largely aligns with the environmental factors from each site. There is little black ash found in Site 1 (Figure 3.11a), except for a swampy portion in the eastern part of the site but white and green ash are present on the site (along with other hardwoods). Conversely, there are significant amounts of black ash found in Site 2 (Figure 3.11b), especially in the south-central portion of the site. The classification product largely aligns with these environmental factors, with relatively more BA classified in Site 2 and relatively more QA and HW in Site 1. The model does seem to be over-predicting QA in Site 1, however, so further refinement is needed.

3.5. Conclusions

Despite the small sample size, we mapped the ash genera and black ash species with relative accuracy using single-date WV-2 imagery, similar to other researchers but in a novel environment. By establishing a working methodology with a clear path forward and known methods to increase the accuracy of the classification, we have shown that using object-based methods and WV-2 multispectral data can provide a viable method of mapping black ash.

CHAPTER 4 CONCLUSIONS AND FUTURE WORK

4.1. Pixel vs. object based classification

Overall, object-based approaches achieved higher accuracy metrics than pixel-based methods while producing maps that more closely align to the landscape realities on the ground using both multispectral and hyperspectral data. While there was significant disagreement between three of the hardwood classes (AS, RM, and HW), this was expected as other researchers have encountered similar results (Lisein et al. 2015; Maschler et al. 2018). All methods over-predict ash to varying extents but, as the goal is to identify as much ash as possible for conservation efforts, that outcome is more desirable than the under-prediction of ash. These classification methods, especially the object-based ones, could serve as a valuable tool to direct field workers and foresters to areas of previously unknown ash, even if those areas have less ash than what the model predicts.

4.2. Hyper- vs. multi- spectral classification

Hyperspectral imagery achieved significantly higher accuracy results than multispectral in both pixel- and object-based classification methods. Given the spectral similarity shown between ash and its co-occurring hardwood species it is unsurprising that hyperspectral imagery outperformed multispectral imagery. Interestingly, black ash showed a significant difference from co-occurring hardwood species that green and white ash did not. As discussed further below, obtaining data in as wide a spectrum as possible would be highly advantageous for the identification of black ash.

4.3. RF vs. SVM

With the exception of hyperspectral object-based SVM classification, there was not a statistically significant difference between the classification algorithms of RF and SVM. That

being said, even when statistically similar, SVM captured more variation in classes than did RF and seemed to be more ecologically realistic based on experiences in the field. With the multispectral data in particular RF classified large contiguous areas of quaking aspen (in Site 1) and softwood (in Site 2) that were not encountered in the field. However, the differences in classification ability were largely not statistically significant, raising the possibility that with additional or different data, RF could provide as accurate a classification as SVM.

4.4. Drawbacks

One of the most critical aspects of this work to be lacking is the sample size. Accuracy increases proportionally with sample size (Sapkota and Liang 2020), with many studies involving a minimum of 50 samples per class (Murfitt et al. 2016; Waser et al. 2014). Field work for this study was completed during the summer of 2020 with the impact of COVID-19 quarantines and social distancing in place and, as such, only one person could be in the field at a time and time in the field was limited. Despite these limitations, 420 canopy trees (as defined by dominant, co-dominant, or intermediate crown class status) were identified and GPS tagged. The translation of field samples to identified and delineated tree crown polygons, however, proved to be significantly difficult.

The greatest hindrance to the positive identification of individual tree crowns was the density and complexity of the forests being studied. In many cases crowns will overlap or, in particularly dense areas, be displaced significantly from the main body of the tree. Black ash trees in particular are able to achieve canopy status while being very small – the average dominant or co-dominant black ash tree tagged in this study was 13.2 cm (5.2 in) DBH, while the average dominant or co-dominant red maple was roughly 24.3 cm (9.6 in) DBH - and is generally known to have a narrow crown (Erdmann et al. 1987; Everett 2019).

Geospatial differences between the remotely sensed and field collected data added a further layer of complication to identifying individual trees. WV-2 imagery has a horizontal accuracy of <3.5m CE90 (DigitalGlobe 2009), meaning that 90% of the imagery will be located within 3.5m of the actual ground location. While this level of accuracy is sufficient for many applications, when dealing with very small tree crowns any additional amount of error can make identification difficult. Finally, tangential scale distortion was observed in the G-LiHT hyperspectral data that made delineation more difficult and frustrated attempts at automation. These differences, while small, impacted the ability to discern trees and highlights the need to have highly precise and co-registered remote sensing and field data.

In addition, this study relied on fine spatial resolution imagery. As the final resolution of both the hyperspectral and multispectral data was very similar (0.6 m vs 0.61 m, respectively), it is unlikely that this impacted the difference in classification accuracies. That being said, the hyperspectral G-LiHT imagery was captured alongside a 0.04 m red-green-blue orthomosaic, which served as a highly valuable reference for the identification of individual tree crowns. Given the highly complex nature of the areas in which black ash tends to grow, obtaining the highest spatial resolution imagery possible would provide the best opportunity for ash classification.

4.5. Areas of further research

Utilizing a time series of images would allow for further refinement of the model, as both ash trees as a genus and black ash in particular show significant seasonal variation. Time series of images have been used in identifying ash previously (Lisein et al. 2015), with the highest accuracies achieved with spring, early summer, and fall images. Ash trees tend to have a shorter foliage season than co-occurring deciduous trees, allowing for early or late season imagery to

easily differentiate ash. Further, black and green ash show a distinct difference in color from white ash in the fall (with black and green turning yellow, while white ash turns purple), adding another possible differentiation point. However, the extra cost associated with such high spatial, spectral, and temporal resolution data can be economically prohibitive on the landscape scale.

In addition, other sensor packages should be considered. Black ash is uniquely (among closely related ash species) able to uptake and release water (Kolka et al. 2018; Slesak et al. 2014), so imagery in the shortwave infrared portions of the electromagnetic spectrum (those more related to water content) would be beneficial. It would be most beneficial, however, to capture imagery during peak water drawdown (and thus peak evapotranspiration). Therefore, it is likely that a time series of imagery captured over a growing season, from bud-break to senescence, and captured from the optical to shortwave infrared range, would have the highest ability to identify black ash.

When aiming to expand this study beyond the study area, the ability of multispectral imagery to identify ash will be key. Given the cost and impracticality of acquiring high resolution hyperspectral imagery over the entire state of Maine, acquiring multispectral imagery is more feasible. Sensors such as WV-3 are able to collect high resolution imagery in both the optical and shortwave infrared regions, making them an ideal candidate for large scale ash mapping. Cost remains an issue, however, and freely available imagery such as that from NAIP should be considered. NAIP imagery, while only providing a single date in four bands (red, green, blue, and near-infrared), has similar spatial resolution (0.6 m) to the imagery used in this study and provides coverage for the entire state.

While not directly addressed in this study, it is possible that the inclusion of certain site variables could increase the accuracy of classification models. Host et al. (2020) and Engelstad et

al. (2019) successfully utilized site variables such as the Compound Topographic Index in classifying ash and black ash dominance, respectively, albeit at a larger scale (30 m spatial resolution) than the current study. It remains to be determined whether the inclusion of such indices will benefit classifications in Maine, however, as the source topographic data may not be captured at a fine enough resolution to capture the subtle variations in terrain that will influence the presence (or lack thereof) of black ash.

To sum up, remotely sensed imagery presents a promising avenue of research for the identification of tree species for conservation purposes. The techniques presented in this study have shown that the identification of ash is possible, if with some confusion between hardwood classes. Furthermore, this research shows that it is possible to identify black ash at the individual tree level. There are a number of paths this research could take to refine the accuracy and broaden the applicability of the models, but it presents a viable workflow and hopeful path forward for ash conservation. With the threat of EAB infestation increasing daily the broad application of this research to Maine would be pivotal to the state's conservation efforts.

WORKS CITED

Aiazzi, B., Baronti, S., Lotti, F., & Selva, M. (2009). A comparison between global and context-adaptive pansharpening of multispectral images. *IEEE Geoscience and Remote Sensing Letters, 6*, 302-306

Amini, S., Homayouni, S., Safari, A., & Darvishsefat, A.A. (2018). Object-based classification of hyperspectral data using Random Forest algorithm. *Geo-spatial information science, 21*, 127-138

Anys, H., Bannari, A., He, D., & Morin, D. (1994). Texture analysis for the mapping of urban areas using airborne MEIS-II images. In, *Proceedings of the First International Airborne Remote Sensing Conference and Exhibition* (pp. 231-245): Environmental Research Institute of Michigan

Barnes, E., Clarke, T., Richards, S., Colaizzi, P., Haberland, J., Kostrzewski, M., Waller, P., Choi, C., Riley, E., & Thompson, T. (2000). Coincident detection of crop water stress, nitrogen status and canopy density using ground based multispectral data. In, *Proceedings of the Fifth International Conference on Precision Agriculture, Bloomington, MN, USA*

Beucher, S. (1982). Watersheds of functions and picture segmentation. In, *ICASSP'82. IEEE International Conference on Acoustics, Speech, and Signal Processing* (pp. 1928-1931): IEEE

Bhattarai, R., Rahimzadeh-Bajgiran, P., Weiskittel, A., & MacLean, D.A. (2020). Sentinel-2 based prediction of spruce budworm defoliation using red-edge spectral vegetation indices. *Remote Sensing Letters, 11*, 777-786

Bhattarai, R., Rahimzadeh-Bajgiran, P., Weiskittel, A., Meneghini, A., & MacLean, D.A. (2021). Spruce budworm tree host species distribution and abundance mapping using multi-temporal Sentinel-1 and Sentinel-2 satellite imagery. *ISPRS Journal of Photogrammetry and Remote Sensing, 172*, 28-40

Blaschke, T., & Hay, G.J. (2001). Object-oriented image analysis and scale-space: theory and methods for modeling and evaluating multiscale landscape structure. *International Archives of Photogrammetry and Remote Sensing, 34*, 22-29

Boardman, J.W., & Kruse, F.A. (2011). Analysis of imaging spectrometer data using $ N $-dimensional geometry and a mixture-tuned matched filtering approach. *IEEE Transactions on Geoscience and Remote Sensing, 49*, 4138-4152

Bolstad, P., Jenks, A., Berkin, J., Horne, K., & Reading, W.H. (2005). A comparison of autonomous, WAAS, real-time, and post-processed global positioning systems (GPS) accuracies in northern forests. *Northern Journal of Applied Forestry, 22*, 5-11

Breiman, L. (2001). Random forests. *Machine learning, 45*, 5-32

Broge, N.H., & Leblanc, E. (2001). Comparing prediction power and stability of broadband and hyperspectral vegetation indices for estimation of green leaf area index and canopy chlorophyll density. *Remote Sensing of Environment, 76*, 156-172

Bryant, E., Dodge, A.G., & Warren, S.D. (1980). Landsat for practical forest type mapping- A test case. *Photogrammetric Engineering and Remote Sensing, 46*, 1575-1584

Bunting, P., & Lucas, R. (2006). The delineation of tree crowns in Australian mixed species forests using hyperspectral Compact Airborne Spectrographic Imager (CASI) data. *Remote Sensing of Environment, 101*, 230-248

Burns, R.M., & Honkala, B.H. (1990). *Silvics of north America*. United States Department of Agriculture Washington, DC

Cappaert, D., McCullough, D.G., Poland, T.M., & Siegert, N.W. (2005). Emerald ash borer in North America: a research and regulatory challenge. *American Entomologist. 51 (3): 152-165., 51*

Cohen, W.B., Healey, S.P., Yang, Z., Stehman, S.V., Brewer, C.K., Brooks, E.B., Gorelick, N., Huang, C., Hughes, M.J., & Kennedy, R.E. (2017). How similar are forest disturbance maps derived from different Landsat time series algorithms? *Forests, 8*, 98

Cook, B., Corp, L., Nelson, R., Middleton, E., Morton, D., McCorkel, J., Masek, J., Ranson, K., Ly, V., & Montesano, P. (2013). NASA Goddard's LiDAR, Hyperspectral and Thermal (G-LiHT) Airborne Imager. *Remote Sensing, 5*, 4045-4066

Cooley, T., Anderson, G.P., Felde, G.W., Hoke, M.L., Ratkowski, A.J., Chetwynd, J.H., Gardner, J.A., Adler-Golden, S.M., Matthew, M.W., & Berk, A. (2002). FLAASH, a MODTRAN4-based atmospheric correction algorithm, its application and validation. In, *IEEE International Geoscience and Remote Sensing Symposium* (pp. 1414-1418): IEEE

Costanza, K. (2015). Growth Response of Fraxinus nigra Marsh (Lamiales: Oleaceae) Used to Predict High-Quality Sites in Maine and Northern New York: An Approach to Prioritizing Preparedness and Management of Agrilus planipennis Fairmaire (Coleoptera: Buprestidae). In, *Forest Resources* (p. 121). Orono, Maine: University of Maine

Costanza, K.K., Livingston, W.H., Kashian, D.M., Slesak, R.A., Tardif, J.C., Dech, J.P., Diamond, A.K., Daigle, J.J., Ranco, D.J., & Neptune, J.S. (2017). The precarious state of a cultural keystone species: tribal and biological assessments of the role and future of black ash. *Journal of Forestry, 115*, 435-446

Crippen, R.E. (1990). Calculating the vegetation index faster. *Remote Sensing of Environment, 34*, 71-73

D'Amato, A., Palik, B., Slesak, R., Edge, G., Matula, C., & Bronson, D. (2018). Evaluating Adaptive Management Options for Black Ash Forests in the Face of Emerald Ash Borer Invasion. *Forests, 9*

Dalponte, M., Ørka, H.O., Ene, L.T., Gobakken, T., & Næsset, E. (2014). Tree crown delineation and tree species classification in boreal forests using hyperspectral and ALS data. *Remote Sensing of Environment, 140*, 306-317

Daughtry, C.S., Walthall, C., Kim, M., De Colstoun, E.B., & McMurtrey Iii, J. (2000). Estimating corn leaf chlorophyll concentration from leaf and canopy reflectance. *Remote Sensing of Environment, 74*, 229-239

DigitalGlobe, I. (2009). the Benefits of the 8 Spectral Bands of WorldView-2. In. www.digitalglobe.com

Engelstad, P.S., Falkowski, M.J., D'Amato, A.W., Slesak, R.A., Palik, B.J., Domke, G.M., & Russell, M.B. (2019). Mapping black ash dominated stands using geospatial and forest inventory data in northern Minnesota, USA. *Canadian Journal of Forest Research, 48*, 892-902

Erdmann, G.G., Crow, T.R., Ralph Jr, M., & Wilson, C.D. (1987). Managing black ash in the Lake States. *General Technical Report NC-115. St. Paul, MN: US Dept. of Agriculture, Forest Service, North Central Forest Experiment Station, 115*

Everett, T. (2019). EAB Response: An Ash Resource Inventory Field Manual. In, *School of Forest Resources* (p. 171): University of Maine

Fassnacht, F.E., Latifi, H., Stereńczak, K., Modzelewska, A., Lefsky, M., Waser, L.T., Straub, C., & Ghosh, A. (2016). Review of studies on tree species classification from remotely sensed data. *Remote Sensing of Environment, 186*, 64-87

Federal Register (2003). Emerald Ash Borer Quarantine and Regulations. In

Ferreira, M.P., Wagner, F.H., Aragão, L.E., Shimabukuro, Y.E., & de Souza Filho, C.R. (2019). Tree species classification in tropical forests using visible to shortwave infrared WorldView-3 images and texture analysis. *ISPRS Journal of Photogrammetry and Remote Sensing, 149*, 119-131

Foody, G.M. (2002). Status of land cover classification accuracy assessment. *Remote Sensing of Environment, 80*, 185-201

Francese, J.A., Booth, E.G., Lopez, V.M., & Sorensen, B. (2019). Alternative survey methods for the emerald ash borer. *Florida Entomologist, 102*, 243-245

Franklin, S., Hall, R., Moskal, L., Maudie, A., & Lavigne, M. (2000). Incorporating texture into classification of forest species composition from airborne multispectral images. *International journal of remote sensing, 21*, 61-79

Gamon, J., Serrano, L., & Surfus, J. (1997). The photochemical reflectance index: an optical indicator of photosynthetic radiation use efficiency across species, functional types, and nutrient levels. *Oecologia, 112*, 492-501

Garzon-Lopez, C.X., & Lasso, E. (2020). Species Classification in a Tropical Alpine Ecosystem Using UAV-Borne RGB and Hyperspectral Imagery. *Drones, 4*, 69

Gitelson, A., & Merzlyak, M.N. (1994). Spectral reflectance changes associated with autumn senescence of Aesculus hippocastanum L. and Acer platanoides L. leaves. Spectral features and relation to chlorophyll estimation. *Journal of plant physiology, 143*, 286-292

Gitelson, A., Stark, R., Grits, U., Rundquist, D., Kaufman, Y., & Derry, D. (2002). Vegetation and soil lines in visible spectral space: a concept and technique for remote estimation of vegetation fraction. *International journal of remote sensing, 23*, 2537-2562

Gitelson, A.A., Kaufman, Y.J., & Merzlyak, M.N. (1996a). Use of a green channel in remote sensing of global vegetation from EOS-MODIS. *Remote Sensing of Environment, 58*, 289-298

Gitelson, A.A., & Merzlyak, M.N. (1998). Remote sensing of chlorophyll concentration in higher plant leaves. *Advances in Space Research, 22*, 689-692

Gitelson, A.A., Merzlyak, M.N., & Chivkunova, O.B. (2001). Optical properties and nondestructive estimation of anthocyanin content in plant leaves¶. *Photochemistry and photobiology, 74*, 38-45

Gitelson, A.A., Merzlyak, M.N., & Lichtenthaler, H.K. (1996b). Detection of red edge position and chlorophyll content by reflectance measurements near 700 nm. *Journal of plant physiology, 148*, 501-508

Gougeon, F.A., & Leckie, D.G. (2006). The individual tree crown approach applied to Ikonos images of a coniferous plantation area. *Photogrammetric Engineering & Remote Sensing, 72*, 1287-1297

Gwata, B. (2012). Developing high resolution clutter for wireless network propagation using WorldView-2 imagery. In, *Algorithms and Technologies for Multispectral, Hyperspectral, and Ultraspectral Imagery XVIII* (p. 83902Q): International Society for Optics and Photonics

Haack, R.A., Jendak, E., Houping, L., Marchant, K.R., Petrice, T.R., Poland, T.M., & Ye, H. (2002). The emerald ash borer: a new exotic pest in North America

Haboudane, D., Miller, J.R., Pattey, E., Zarco-Tejada, P.J., & Strachan, I.B. (2004). Hyperspectral vegetation indices and novel algorithms for predicting green LAI of crop canopies: Modeling and validation in the context of precision agriculture. *Remote Sensing of Environment, 90*, 337-352

Hall, R., Castilla, G., White, J., Cooke, B., & Skakun, R. (2016). Remote sensing of forest pest damage: a review and lessons learned from a Canadian perspective. *The Canadian Entomologist, 148*, S296-S356

Haralick, R.M., Shanmugam, K., & Dinstein, I.H. (1973). Textural features for image classification. *IEEE Transactions on systems, man, and cybernetics*, 610-621

Herms, D.A., & McCullough, D.G. (2014). Emerald ash borer invasion of North America: history, biology, ecology, impacts, and management. *Annu Rev Entomol, 59*, 13-30

Host, T.K., Russell, M.B., Windmuller-Campione, M.A., Slesak, R.A., & Knight, J.F. (2020). Ash Presence and Abundance Derived from Composite Landsat and Sentinel-2 Time Series and Lidar Surface Models in Minnesota, USA. *Remote Sensing, 12*, 1341

Huete, A., Justice, C., & Liu, H. (1994). Development of vegetation and soil indices for MODIS-EOS. *Remote Sensing of Environment, 49*, 224-234

Immitzer, M., Atzberger, C., & Koukal, T. (2012). Tree Species Classification with Random Forest Using Very High Spatial Resolution 8-Band WorldView-2 Satellite Data. *Remote Sensing, 4*, 2661-2693

Ishimura, A., Shimizu, Y., Rahimzadeh-Bajgiran, P., & Omasa, K. (2011). Remote sensing of Japanese beech forest decline using an improved Temperature Vegetation Dryness Index (iTVDI). *iForest*, 4 (5), 195–199

Jiang, Z., Huete, A.R., Didan, K., & Miura, T. (2008). Development of a two-band enhanced vegetation index without a blue band. *Remote Sensing of Environment, 112*, 3833-3845

Jin, X. (2012). Segmentation-based image processing system. In: Google Patents

Jones, H.G., & Vaughan, R.A. (2010). *Remote sensing of vegetation: principles, techniques, and applications*. Oxford university press

Jordan, C.F. (1969). Derivation of leaf-area index from quality of light on the forest floor. *Ecology, 50,* 663-666

Kaufman, Y.J., & Tanre, D. (1992). Atmospherically resistant vegetation index (ARVI) for EOS-MODIS. *IEEE Transactions on Geoscience and Remote Sensing, 30,* 261-270

Kennedy, H.E. (1990). Green ash. *Silvics of North America*. Washington, DC: United States Department of Agriculture

Kim, M., Madden, M., & Warner, T.A. (2009). Forest type mapping using object-specific texture measures from multispectral Ikonos imagery. *Photogrammetric Engineering & Remote Sensing, 75,* 819-829

Klooster, W., Gandhi, K., Long, L., Perry, K., Rice, K., & Herms, D. (2018). Ecological Impacts of Emerald Ash Borer in Forests at the Epicenter of the Invasion in North America. *Forests, 9*

Klooster, W.S., Herms, D.A., Knight, K.S., Herms, C.P., McCullough, D.G., Smith, A., Gandhi, K.J., & Cardina, J. (2014). Ash (Fraxinus spp.) mortality, regeneration, and seed bank dynamics in mixed hardwood forests following invasion by emerald ash borer (Agrilus planipennis). *Biological Invasions, 16,* 859-873

Knight, K.S., Brown, J.P., & Long, R.P. (2013). Factors affecting the survival of ash (Fraxinus spp.) trees infested by emerald ash borer (Agrilus planipennis). *Biological Invasions, 15,* 371-383

Kolka, R.K., D'Amato, A.W., Wagenbrenner, J.W., Slesak, R.A., Pypker, T.G., Youngquist, M.B., Grinde, A.R., & Palik, B.J. (2018). Review of ecosystem level impacts of emerald ash borer on black ash wetlands: what does the future hold? *Forests, 9,* 179

Kovacs, K.F., Haight, R.G., McCullough, D.G., Mercader, R.J., Siegert, N.W., & Liebhold, A.M. (2010). Cost of potential emerald ash borer damage in US communities, 2009–2019. *Ecological Economics, 69,* 569-578

Le Maire, G., Francois, C., & Dufrene, E. (2004). Towards universal broad leaf chlorophyll indices using PROSPECT simulated database and hyperspectral reflectance measurements. *Remote Sensing of Environment, 89,* 1-28

Li, J., Hu, B., & Woods, M. (2015). A Two-Level Approach for Species Identification of Coniferous Trees in Central Ontario Forests Based on Multispectral Images. *IEEE Journal of Selected Topics in Applied Earth Observations and Remote Sensing, 8,* 1487-1497

Lisein, J., Michez, A., Claessens, H., & Lejeune, P. (2015). Discrimination of Deciduous Tree Species from Time Series of Unmanned Aerial System Imagery. *PLoS ONE, 10,* e0141006

Liu, H. (2017). Ash Tree Identification Based on the Integration of Hyperspectral Imagery and High-density Lidar Data

Liu, H.Q., & Huete, A. (1995). A feedback based modification of the NDVI to minimize canopy background and atmospheric noise. *IEEE Transactions on Geoscience and Remote Sensing, 33*, 457-465

Lu, D., & Weng, Q. (2007). A survey of image classification methods and techniques for improving classification performance. *International journal of remote sensing, 28*, 823-870

Ma, L., Li, M., Ma, X., Cheng, L., Du, P., & Liu, Y. (2017). A review of supervised object-based land-cover image classification. *ISPRS Journal of Photogrammetry and Remote Sensing, 130*, 277-293

Maine Forest Service (2018). Emerald Ash Borer Discovered in Maine. In. Augusta, ME

Maine Forest Service (2020). Monitoring for EAB with Traps. In Maine Department of Agriculture Conservation & Forestry (Ed.)

Marrs, J., & Ni-Meister, W. (2019). Machine Learning Techniques for Tree Species Classification Using Co-Registered LiDAR and Hyperspectral Data. *Remote Sensing, 11*

Maschler, J., Atzberger, C., & Immitzer, M. (2018). Individual tree crown segmentation and classification of 13 tree species using airborne hyperspectral data. *Remote Sensing, 10*, 1218

Mercader, R.J., Siegert, A.M., Liebhold, A.M., & McCullough, D.G. (2009). Dispersal of the emerald ash borer, Agrilus planipennis, in newly-colonized sites. *Agricultural and Forest Entomology. 11: 421? 424., 11*

Mercader, R.J., Siegert, N.W., Liebhold, A.M., & McCullough, D.G. (2011). Influence of foraging behavior and host spatial distribution on the localized spread of the emerald ash borer, Agrilus planipennis. *Population Ecology, 53*, 271-285

Merzlyak, M.N., Gitelson, A.A., Chivkunova, O.B., & Rakitin, V.Y. (1999). Non-destructive optical detection of pigment changes during leaf senescence and fruit ripening. *Physiologia plantarum, 106*, 135-141

Merzlyak, M.N., Solovchenko, A.E., & Gitelson, A.A. (2003). Reflectance spectral features and non-destructive estimation of chlorophyll, carotenoid and anthocyanin content in apple fruit. *Postharvest biology and technology, 27*, 197-211

Murfitt, J., He, Y., Yang, J., Mui, A., & De Mille, K. (2016). Ash Decline Assessment in Emerald Ash Borer Infested Natural Forests Using High Spatial Resolution Images. *Remote Sensing, 8*

Myint, S.W., Gober, P., Brazel, A., Grossman-Clarke, S., & Weng, Q. (2011). Per-pixel vs. object-based classification of urban land cover extraction using high spatial resolution imagery. *Remote Sensing of Environment, 115*, 1145-1161

Nitze, I., Schulthess, U., & Asche, H. (2012). Comparison of machine learning algorithms random forest, artificial neural network and support vector machine to maximum likelihood for supervised crop type classification. *Proc. of the 4th GEOBIA, 35*

Noble, W.S. (2006). What is a support vector machine? *Nature biotechnology, 24*, 1565-1567

Penuelas, J., Filella, I., & Gamon, J.A. (1995). Assessment of photosynthetic radiation-use efficiency with spectral reflectance. *New Phytologist, 131*, 291-296

Poland, T.M., & McCullough, D.G. (2006). Emerald ash borer: invasion of the urban forest and the threat to North America's ash resource. *Journal of Forestry, 104*, 118-124

Poland, T.M., Petrice, T.R., & Ciaramitaro, T.M. (2019). Trap designs, colors, and lures for emerald ash borer detection. *Frontiers in Forests and Global Change, 2*, 80

Pontius, J. (2014). A new approach for forest decline assessments: maximizing detail and accuracy with multispectral imagery. *International journal of remote sensing, 35*, 3384-3402

Pontius, J., Hanavan, R.P., Hallett, R.A., Cook, B.D., & Corp, L.A. (2017). High spatial resolution spectral unmixing for mapping ash species across a complex urban environment. *Remote Sensing of Environment, 199*, 360-369

Pontius, J., Martin, M., Plourde, L., & Hallett, R. (2008). Ash decline assessment in emerald ash borer-infested regions: A test of tree-level, hyperspectral technologies. *Remote Sensing of Environment, 112*, 2665-2676

Prasad, A.M., Iverson, L.R., Peters, M.P., Bossenbroek, J.M., Matthews, S.N., Sydnor, T.D., & Schwartz, M.W. (2010). Modeling the invasive emerald ash borer risk of spread using a spatially explicit cellular model. *Landscape ecology, 25*, 353-369

R Core Team (2020). R: A Language and Environment for Statistical Computing. In. Vienna, Austria: R Foundation for Statistical Computing

Rahimzadeh-Bajgiran, P., Hennigar, C., Weiskittel, A., & Lamb, S. (2020). Forest potential productivity mapping by linking remote-sensing-derived metrics to site variables. *Remote Sensing, 12*, 2056

Rahimzadeh-Bajgiran, P., Weiskittel, A.R., Kneeshaw, D., & MacLean, D.A. (2018). Detection of annual spruce budworm defoliation and severity classification using Landsat imagery. *Forests, 9*, 357

Rebek, E.J., Herms, D.A., & Smitley, D.R. (2008). Interspecific variation in resistance to emerald ash borer (Coleoptera: Buprestidae) among North American and Asian ash (Fraxinus spp.). *Environmental entomology, 37*, 242-246

Rondeaux, G., Steven, M., & Baret, F. (1996). Optimization of soil-adjusted vegetation indices. *Remote Sensing of Environment, 55*, 95-107

Roujean, J.-L., & Breon, F.-M. (1995). Estimating PAR absorbed by vegetation from bidirectional reflectance measurements. *Remote Sensing of Environment, 51*, 375-384

Rouse, J., Haas, R.H., Schell, J.A., & Deering, D.W. (1974). Monitoring vegetation systems in the Great Plains with ERTS. *NASA special publication, 351*, 309

Russell, M.B., & Weiskittel, A.R. (2011). Maximum and largest crown width equations for 15 tree species in Maine. *Northern Journal of Applied Forestry, 28*, 84-91

Sapkota, B.B., & Liang, L. (2020). High-Resolution Mapping of Ash (Fraxinus spp.) in Bottomland Hardwoods to Slow Emerald Ash Borer Infestation. *Science of Remote Sensing*, 100004

Shruthi, R.B., Kerle, N., Jetten, V., & Stein, A. (2014). Object-based gully system prediction from medium resolution imagery using Random Forests. *Geomorphology, 216*, 283-294

Siegert, N.W., McCullough, D.G., Liebhold, A.M., & Telewski, F.W. (2014). Dendrochronological reconstruction of the epicentre and early spread of emerald ash borer in North America. *Diversity and Distributions, 20*, 847-858

Sims, D.A., & Gamon, J.A. (2002). Relationships between leaf pigment content and spectral reflectance across a wide range of species, leaf structures and developmental stages. *Remote Sensing of Environment, 81*, 337-354

Slesak, R.A., Lenhart, C.F., Brooks, K.N., D'Amato, A.W., & Palik, B.J. (2014). Water table response to harvesting and simulated emerald ash borer mortality in black ash wetlands in Minnesota, USA. *Canadian Journal of Forest Research, 44*, 961-968

Sohn, Y., & Rebello, N.S. (2002). Supervised and unsupervised spectral angle classifiers. *Photogrammetric Engineering and Remote Sensing, 68*, 1271-1282

Steiner, K.C., Graboski, L.E., Knight, K.S., Koch, J.L., & Mason, M.E. (2019). Genetic, spatial, and temporal aspects of decline and mortality in a Fraxinus provenance test following invasion by the emerald ash borer. *Biological Invasions, 21*, 3439-3450

Sydnor, T.D., Bumgardner, M., & Subburayalu, S. (2011). Community ash densities and economic impact potential of emerald ash borer (Agrilus planipennis) in four Midwestern states. *Aboriculture & Urban Forestry. 37 (2): 84-89.*, 84-89

Tardif, J., Dery, S., & Bergeron, Y. (1994). Sexual regeneration of black ash (Fraxinus nigra Marsh.) in a boreal floodplain. *American Midland Naturalist*, 124-135

Taylor, R.A., Poland, T.M., Bauer, L.S., Windell, K.N., & Kautz, J.L. (2007). Emerald ash borer flight estimates revised. *Proceedings of the emerald ash borer/Asian longhorned beetle research and Te. FHTET-2007-04. US Department of Agriculture Forest Service, Forest Health Technology Enterprise Team, Morgantown*, 10

Team, R. (2015). RStudio: integrated development for R. *RStudio, Inc., Boston, MA URL http://www. rstudio. com, 42*, 14

Thanh Noi, P., & Kappas, M. (2018). Comparison of random forest, k-nearest neighbor, and support vector machine classifiers for land cover classification using Sentinel-2 imagery. *Sensors, 18*, 18

Thapa, B., Wolter, P.T., Sturtevant, B.R., & Townsend, P.A. (2020). Reconstructing past forest composition and abundance by using archived Landsat and national forest inventory data. *International journal of remote sensing, 41*, 4022-4056

Tucker, C.J. (1979). Red and photographic infrared linear combinations for monitoring vegetation. *Remote Sensing of Environment, 8*, 127-150

USDA Forest Service (2018). Individual Tree Species Parameter Maps. In. https://data.nal.usda.gov/dataset/individual-tree-species-parameter-maps.: USDA Forest Service,

Vogelmann, J., Rock, B., & Moss, D. (1993). Red edge spectral measurements from sugar maple leaves. *TitleREMOTE SENSING, 14*, 1563-1575

Wang, D., Wan, B., Qiu, P., Su, Y., Guo, Q., & Wu, X. (2018). Artificial mangrove species mapping using pléiades-1: An evaluation of pixel-based and object-based classifications with selected machine learning algorithms. *Remote Sensing, 10*, 294

Waser, L., Küchler, M., Jütte, K., & Stampfer, T. (2014). Evaluating the Potential of WorldView-2 Data to Classify Tree Species and Different Levels of Ash Mortality. *Remote Sensing, 6*, 4515-4545

Wolf, A.F. (2012). Using WorldView-2 Vis-NIR multispectral imagery to support land mapping and feature extraction using normalized difference index ratios. In, *Algorithms and Technologies for Multispectral, Hyperspectral, and Ultraspectral Imagery XVIII* (p. 83900N): International Society for Optics and Photonics

Wolter, P.T., & Townsend, P.A. (2011). Multi-sensor data fusion for estimating forest species composition and abundance in northern Minnesota. *Remote Sensing of Environment, 115*, 671-691

Wright, J.W., & Rauscher, H.M. (1990). Black ash. *Silvics of North America*. Washington, DC: United States Department of Agriculture

Wu, C., Niu, Z., Tang, Q., & Huang, W. (2008). Estimating chlorophyll content from hyperspectral vegetation indices: Modeling and validation. *Agricultural and forest meteorology, 148*, 1230-1241

Xue, J., & Su, B. (2017). Significant remote sensing vegetation indices: A review of developments and applications. *Journal of sensors, 2017*

Yang, J., He, Y., & Caspersen, J. (2014a). A multi-band watershed segmentation method for individual tree crown delineation from high resolution multispectral aerial image. In, *2014 IEEE Geoscience and Remote Sensing Symposium* (pp. 1588-1591): IEEE

Yang, J., He, Y., Caspersen, J., & Jones, T. (2015). A discrepancy measure for segmentation evaluation from the perspective of object recognition. *ISPRS Journal of Photogrammetry and Remote Sensing, 101*, 186-192

Yang, J., Li, P., & He, Y. (2014b). A multi-band approach to unsupervised scale parameter selection for multi-scale image segmentation. *ISPRS Journal of Photogrammetry and Remote Sensing, 94*, 13-24

Youngquist, M.B., Eggert, S.L., D'Amato, A.W., Palik, B.J., & Slesak, R.A. (2017). Potential effects of foundation species loss on wetland communities: a case study of black ash wetlands threatened by emerald ash borer. *Wetlands, 37*, 787-799

Zhang, K., Hu, B., Hanou, I., & Jin, L. (2012). Early Detecting Ash Emeral Ash Borer (EAB) Infestation Using Hyperspectral Imagery. *IGARSS*, 6360-6363

Zoleikani, R., Zoej, M.V., & Mokhtarzadeh, M. (2017). Comparison of pixel and object oriented based classification of hyperspectral pansharpened images. *Journal of the Indian Society of Remote Sensing, 45*, 25-33

BIOGRAPHY OF THE AUTHOR

John Wells Furniss was born in Rocky Hill, Connecticut on September 10, 1989, and was raised there. He graduated from The Loomis Chaffee School in 2007 before attending Elon University and graduating with a Bachelor's degree in Biology. He then worked as a paralegal, community outreach coordinator, and fundraising coordinator in the New York City area before entering The University of Maine School of Forest Resources graduate school in 2018 and joining Dr. Rahimzadeh-Bajgiran's lab in 2019. John is a candidate for the Master of Science degree in Forest Resources from the University of Maine in August 2021.